Online Supplement to "Prediction of bubbles in presence of α-stable aggregates moving averages"

Gilles de Truchis, Sébastien Fries, Arthur Thomas

This Online Supplement accompanies the main paper by providing two categories of complementary results. First, Section S.1 collects the complete subsampling diagnostics that complement the summary in Section 4.3 of the main text. Second, Section S.2 presents the detailed per-component forecasting results for the OVX application summarized in Section 5.

The supplement is organized as follows. Section S.1 presents the subsampling diagnostics and convergence analysis. Section S.1.2 reports the full results in the original parameter space $\theta = (\rho_1, \rho_2, \varsigma_1, \varsigma_2, \alpha)$, documenting the persistent identification difficulties of the individual scale parameters ς_1 and ς_2 that motivate the reparameterization adopted in the main text. Section S.1.3 presents the corresponding results in the reparameterized space $\vartheta = (\rho_1, \rho_2, \sigma, \pi_1, \alpha)$ defined in equation (4.5) of the main paper, where $\sigma = \varsigma_1 + \varsigma_2$ and $\pi_1 = \varsigma_1/\sigma$. Section S.1.5 reports the restricted subsampling diagnostics under the constraint $\pi_1 = 1/2$, which reduces the parameter vector to $\theta_R = (\rho_1, \rho_2, \sigma, \alpha)$. Section S.1.6 repeats the restricted analysis under the true constraint $\pi_1 = 0.4375$, thereby isolating finite-sample convergence effects from specification bias.

Each subsection contains descriptive statistics, normality test rejection rates, confidence interval coverage, and graphical diagnostics (histograms, Q-Q plots, and kernel density estimates) for all sample sizes. Section S.2 provides the detailed per-component crash probability profiles, in-sample prediction table, and forecast trajectories for the 2020 OVX bubble episode, including the complete algorithm description and discussion of the role of each latent component in the observed volatility dynamics.

S.1. Subsampling Diagnostics and Convergence Analysis

S.1.1. Subsampling methodology

This section describes the subsampling procedure used to assess the finite-sample convergence of our minimum distance estimator toward the limiting normal distribution predicted by Proposition 2.1 of the main paper. The methodology follows Politis and Romano (1994) and Politis et al. (1999) and provides a nonparametric way to evaluate the sampling distribution of $\sqrt{n}(\hat{\theta}_n - \theta_0)$ without requiring explicit knowledge of the asymptotic variance matrix $\Sigma^{-1}\Omega\Sigma^{-1}$.

Given a full sample of size n, we construct non-overlapping subsamples of size $b < n$:

$$\mathcal{X}_b^{(i)} = \{\mathcal{X}_{(i-1)b+1}, \ldots, \mathcal{X}_{ib}\}, \quad i = 1, \ldots, N_b = \lfloor n/b \rfloor. \tag{S.1}$$

Following Politis et al. (1999), we set $b = \lfloor n^{2/3} \rfloor$, which ensures that $b \to \infty$, $b/n \to 0$, and satisfies the higher-order requirements for the subsampling approximation to be valid under weak dependence.

Since the individual scale parameters ς_1 and ς_2 exhibit poor finite-sample convergence in the original parameterization (see Section S.1.2 below), we apply a post-estimation reparameterization:

$$\vartheta = (\rho_1, \rho_2, \sigma, \pi_1, \alpha), \quad \text{where} \quad \sigma = \varsigma_1 + \varsigma_2, \quad \pi_1 = \frac{\varsigma_1}{\sigma}. \tag{S.2}$$

The scaled subsample deviations are then constructed as

$$Z_b^{(i)} = \sqrt{b}\left(\hat{\vartheta}_b^{(i)} - \hat{\vartheta}_n\right), \quad i = 1, \ldots, N_b, \tag{S.3}$$

where $\hat{\vartheta}_n$ is the full-sample MDE estimator mapped to the reparameterized space. Under the conditions of Proposition 2.1, and following the theoretical framework of Politis and Romano (1994), these scaled deviations should approximately follow the same asymptotic distribution as $\sqrt{n}(\hat{\vartheta}_n - \vartheta_0)$.

For each Monte Carlo replication $m = 1, \ldots, M$ and a given sample size n, we proceed as follows:

(ι) Generate a time series $\mathcal{X}_t$ from the true model with parameters θ_0.

($\iota\iota$) Compute the full-sample MDE estimator $\hat{\theta}_n$ and map it to the reparameterized space $\hat{\vartheta}_n$.

($\iota\iota\iota$) Extract $N_b = \lfloor n/b \rfloor$ non-overlapping subsamples with $b = \lfloor n^{2/3} \rfloor$.

($\iota\nu$) For each subsample $i = 1, \ldots, N_b$, compute the subsample estimator $\hat{\vartheta}_b^{(i)}$.

(ν) Construct the scaled deviations $Z_b^{(i)}$ according to (S.3).

The pooled non-overlapping block deviations across all Monte Carlo replications are subjected to several normality diagnostics for each parameter component. First, we compute summary statistics including the sample mean, standard deviation, skewness, and excess kurtosis. Second, we report the Shapiro-Wilk (SW) and Jarque-Bera (JB) rejection rates at the 5% significance level. Third, we assess confidence interval coverage using both quantile-based and normal-approximation intervals at the 90% and 95% levels; for this purpose, confidence intervals are constructed from thinned overlapping blocks (using all $n - b + 1$ overlapping subsamples with appropriate thinning to reduce dependence), while normality diagnostics use the non-overlapping blocks to avoid dependence contamination.

S.1.2. Unrestricted subsampling in the original parameterization

This subsection reports the full subsampling diagnostics when estimation is performed in the original parameter space $\theta = (\rho_1, \rho_2, \varsigma_1, \varsigma_2, \alpha)$, without the reparameterization (σ, π_1) and without any restriction. Tables S.2–S.7 display the scaled subsample deviation statistics, normality test rejection rates, and confidence interval coverage for each sample size. Figures S.1–S.6 provide the corresponding graphical diagnostics. For each parameter and sample size, histograms, Q-Q plots, and kernel density estimates of the standardized non-overlapping block deviations are displayed.

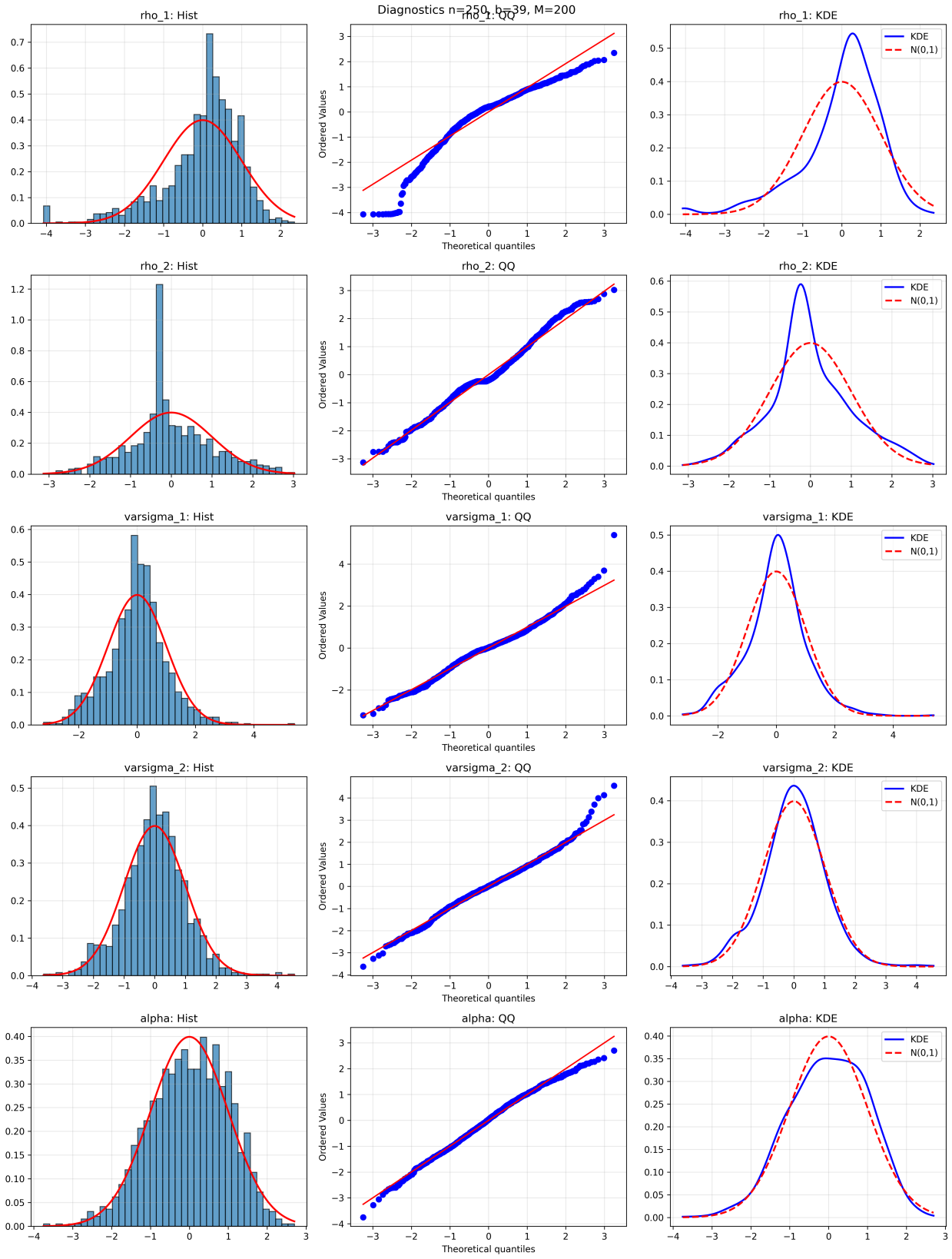

Figure S.1: Diagnostic plots for scaled subsample deviations (original parameterization) at $n = 250$. For each parameter (rows): histogram with standard normal overlay (left), Q-Q plot (center), and kernel density estimate vs. $\mathcal{N}(0, 1)$ (right).

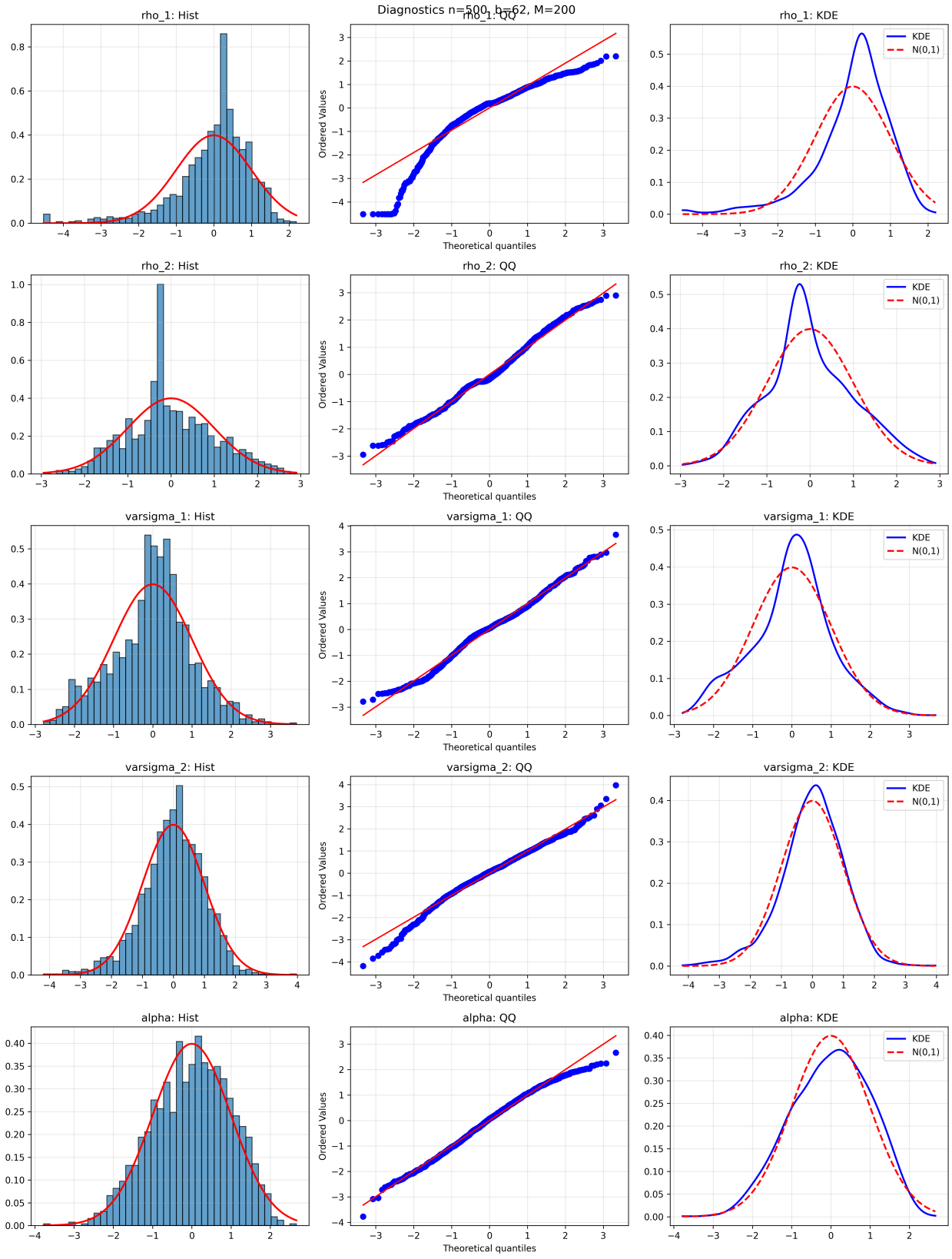

Figure S.2: Diagnostic plots for scaled subsample deviations (original parameterization) at $n = 500$. See caption to Figure S.1 for details.

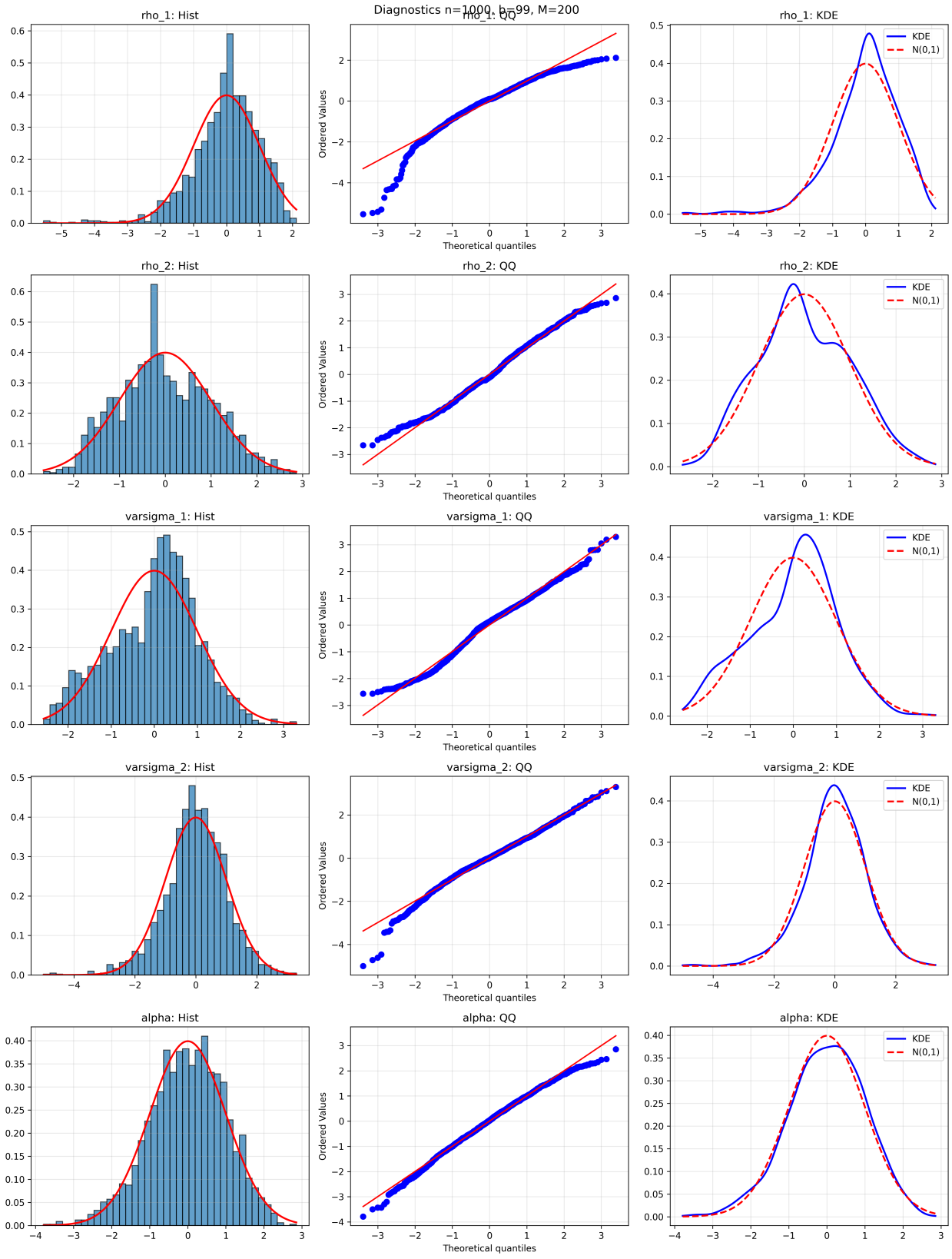

Figure S.3: Diagnostic plots for scaled subsample deviations (original parameterization) at $n = 1,000$. See caption to Figure S.1 for details.

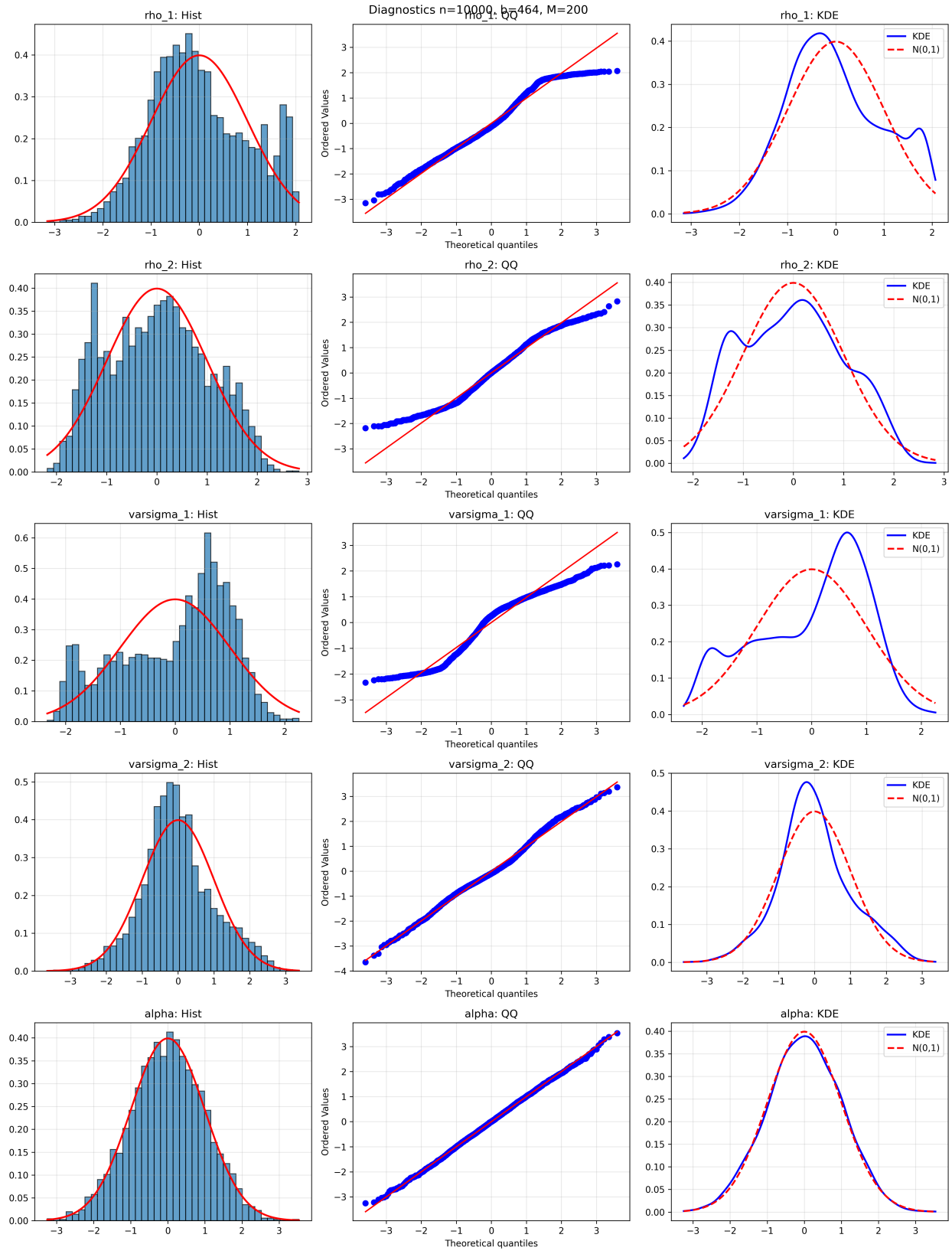

Figure S.4: Diagnostic plots for scaled subsample deviations (original parameterization) at $n = 10,000$. See caption to Figure S.1 for details.

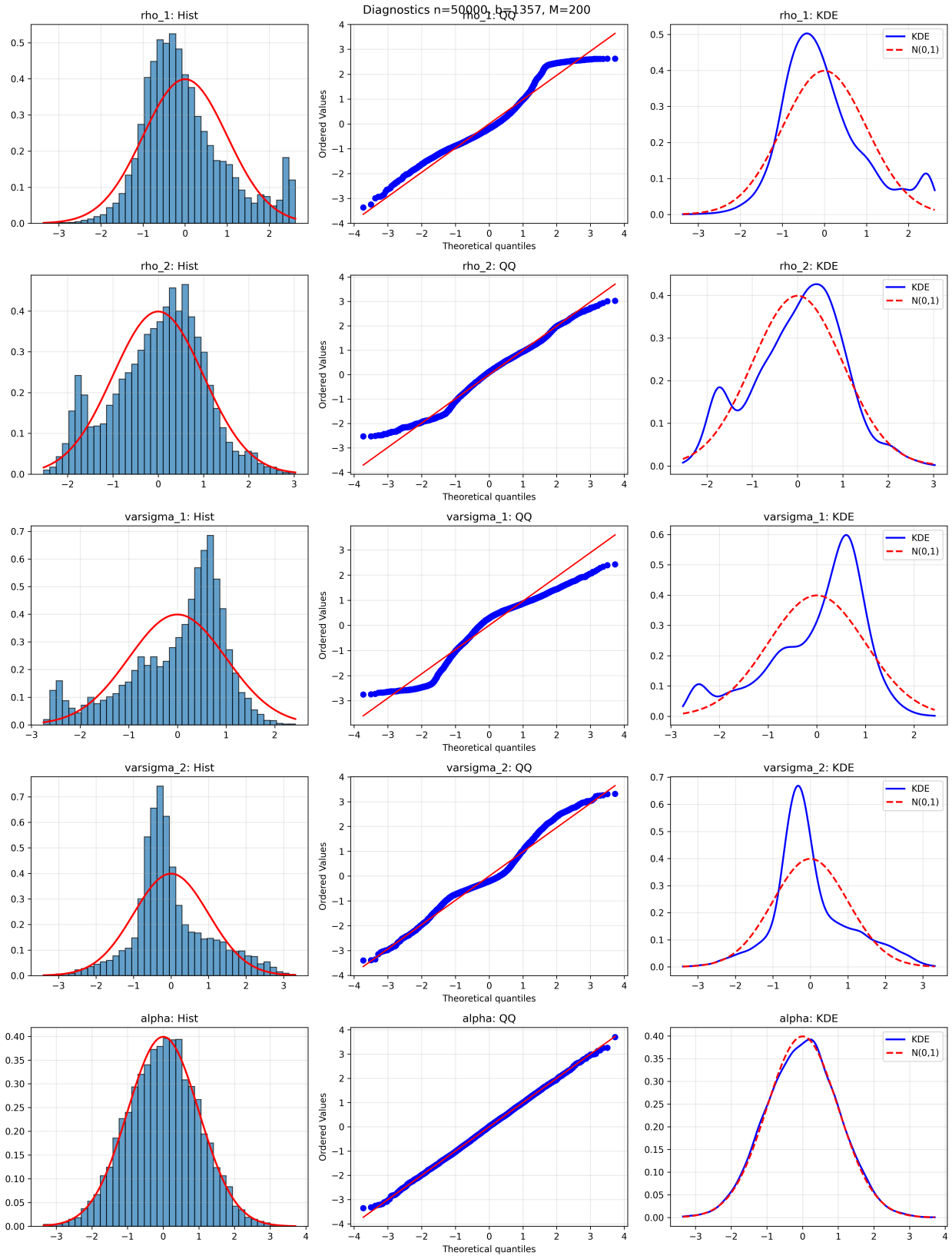

Figure S.5: Diagnostic plots for scaled subsample deviations (original parameterization) at $n = 50,000$. See caption to Figure S.1 for details. .

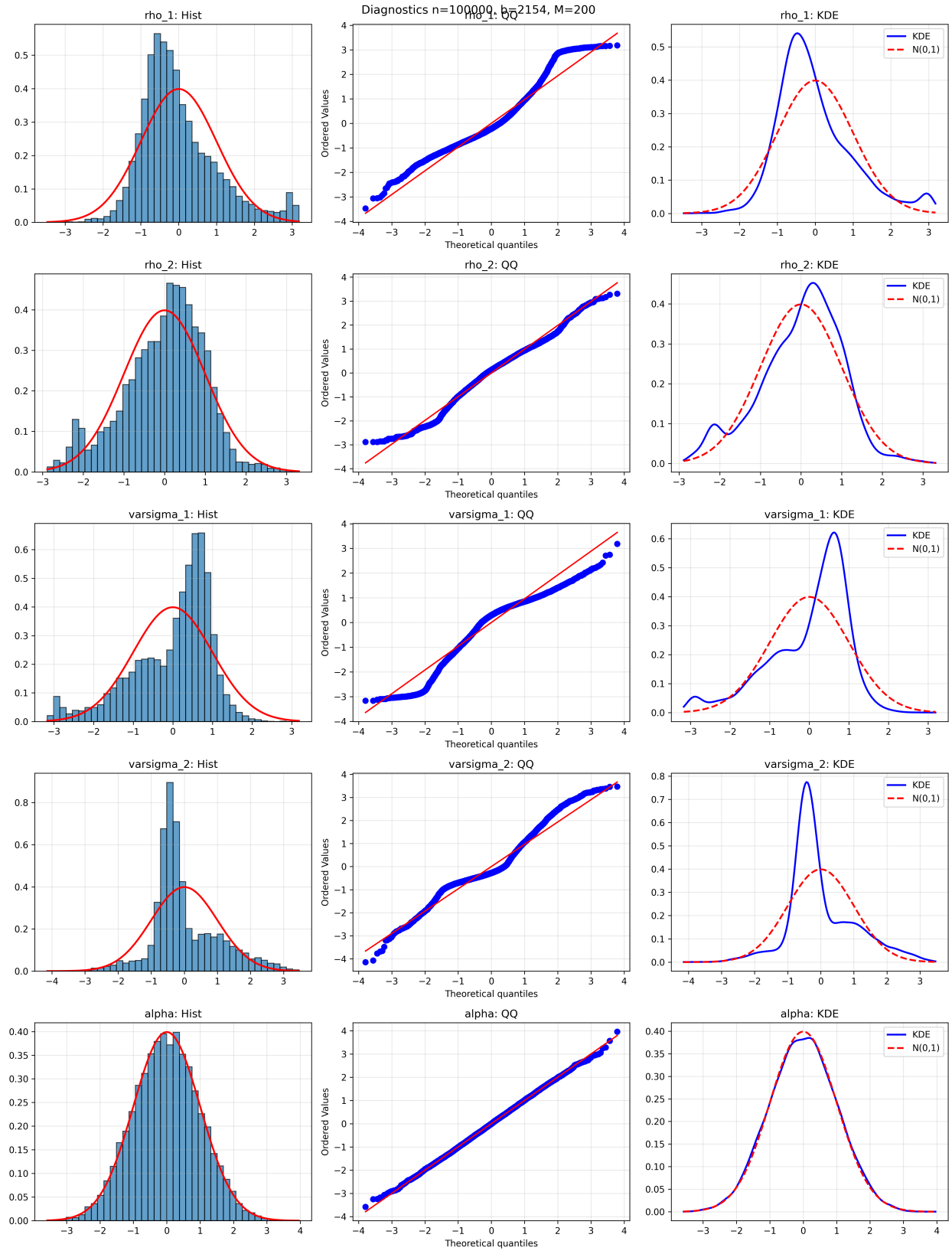

Figure S.6: Diagnostic plots for scaled subsample deviations (original parameterization) at $n = 100,000$. See caption to Figure S.1 for details.

Table S.1: Monte Carlo Design Parameters

Sample Size n	Subsample Size b	Non-overlapping Blocks N_b	MC Replications M
250	39	6	200
500	62	8	200
1,000	99	10	200
10,000	464	21	200
50,000	1,357	36	200
100,000	2,154	46	200

Notes: The subsample size is set to $b = \lfloor n^{2/3} \rfloor$ following Politis et al. (1999). $N_b = \lfloor n/b \rfloor$ denotes the number of non-overlapping blocks per replication.

Table S.2: Subsampling results (original parameterization) for $n = 250$ ($b = 39$, $N_b = 6$, $M = 200$)

									Quantile CI		Normal CI		
Parameter	True	Avg Est.	Std Est.	Dev. Mean	Dev. Std	Skew	Kurt	SW Rej.	JB Rej.	qCov90	qCov95	nCov90	nCov95
ρ_1	0.800	0.782	0.128	−0.309	1.327	−0.518	−0.748	0.175	0.000	0.620	0.630	0.720	0.790
ρ_2	0.300	0.304	0.240	0.390	1.493	0.190	−0.931	0.230	0.000	0.270	0.290	0.355	0.435
ς_1	0.700	0.696	0.385	−0.103	2.466	0.097	−0.787	0.180	0.000	0.280	0.310	0.420	0.485
ς_2	0.900	0.830	0.209	−0.042	1.928	−0.067	−0.751	0.055	0.000	0.600	0.665	0.590	0.685
α	1.500	1.483	0.162	0.253	2.067	−0.107	−0.920	0.065	0.000	0.650	0.690	0.795	0.870

Notes: All results are in the original parameter space $(\rho_1, \rho_2, \varsigma_1, \varsigma_2, \alpha)$ without reparameterization or restriction. SW and JB rejection rates are at the 5% level. qCov and nCov denote quantile-based and normal-approximation CI coverage. Confidence intervals are constructed from thinned overlapping blocks; normality diagnostics use non-overlapping blocks.

S.1.3. Unrestricted subsampling in the reparameterized space

We now report the subsampling diagnostics in the reparameterized space $\vartheta = (\rho_1, \rho_2, \sigma, \pi_1, \alpha)$, where $\sigma = \varsigma_1 + \varsigma_2$ and $\pi_1 = \varsigma_1/\sigma$. Estimation is performed in the original $(\varsigma_1, \varsigma_2)$ space; the transformation is applied post-estimation. We compute scaled subsample deviations $\sqrt{b}(\hat{\vartheta}_b^{(i)} - \hat{\vartheta}_n)$ using non-overlapping blocks of size $b = \lfloor n^{2/3} \rfloor$. For each sample size $n \in \{250, 500, 1,000, 10,000, 50,000, 100,000\}$, we generate $M = 200$ Monte Carlo replications and compute $N_b = \lfloor n/b \rfloor$ non-overlapping blocks per replication. Confidence interval coverage is assessed using all $n - b + 1$ overlapping blocks per replication. The descriptive statistics in Tables S.8–S.13 report the mean, standard deviation, skewness, and excess kurtosis of the non-overlapping block deviations, alongside the Shapiro-Wilk (SW) and Jarque-Bera (JB) rejection rates at the 5% significance level, and the average coverage of 90% and 95% confidence intervals (both quantile-based and normal-

Table S.3: Subsampling results (original parameterization) for $n = 500$ ($b = 62$, $N_b = 8$, $M = 200$)

									Quantile CI		Normal CI		
Parameter	True	Avg Est.	Std Est.	Dev. Mean	Dev. Std	Skew	Kurt	SW Rej.	JB Rej.	qCov90	qCov95	nCov90	nCov95
ρ_1	0.800	0.804	0.111	−0.312	1.499	−0.565	−0.433	0.295	0.045	0.585	0.630	0.635	0.750
ρ_2	0.300	0.297	0.198	0.528	1.960	0.151	−0.762	0.315	0.020	0.395	0.400	0.525	0.575
ς_1	0.700	0.673	0.354	−0.303	2.988	0.111	−0.747	0.235	0.035	0.280	0.285	0.440	0.550
ς_2	0.900	0.849	0.194	−0.030	2.185	−0.144	−0.646	0.080	0.000	0.475	0.545	0.475	0.600
α	1.500	1.489	0.113	0.209	2.404	−0.169	−0.780	0.075	0.000	0.765	0.810	0.855	0.915

Notes: See notes to Table S.2.

Table S.4: Subsampling results (original parameterization) for $n = 1,000$ ($b = 99$, $N_b = 10$, $M = 200$)

									Quantile CI		Normal CI		
Parameter	True	Avg Est.	Std Est.	Dev. Mean	Dev. Std	Skew	Kurt	SW Rej.	JB Rej.	qCov90	qCov95	nCov90	nCov95
ρ_1	0.800	0.812	0.086	−0.152	1.564	−0.415	−0.616	0.260	0.015	0.565	0.605	0.680	0.755
ρ_2	0.300	0.296	0.157	0.573	2.530	0.062	−0.963	0.300	0.010	0.445	0.465	0.600	0.655
ς_1	0.700	0.662	0.301	−0.641	3.757	−0.002	−0.836	0.265	0.020	0.330	0.335	0.445	0.535
ς_2	0.900	0.881	0.163	0.096	2.391	−0.055	−0.382	0.045	0.005	0.420	0.545	0.480	0.585
α	1.500	1.493	0.093	0.128	2.493	−0.153	−0.586	0.045	0.010	0.795	0.815	0.825	0.890

Notes: See notes to Table S.2.

Table S.5: Subsampling results (original parameterization) for $n = 10,000$ ($b = 464$, $N_b = 21$, $M = 200$)

									Quantile CI		Normal CI		
Parameter	True	Avg Est.	Std Est.	Dev. Mean	Dev. Std	Skew	Kurt	SW Rej.	JB Rej.	qCov90	qCov95	nCov90	nCov95
ρ_1	0.800	0.786	0.029	0.427	2.386	0.177	−0.700	0.255	0.010	0.530	0.650	0.770	0.890
ρ_2	0.300	0.260	0.055	1.148	4.591	0.089	−0.973	0.265	0.000	0.505	0.520	0.710	0.825
ς_1	0.700	0.758	0.109	−2.362	7.256	−0.433	−0.892	0.485	0.010	0.290	0.360	0.555	0.750
ς_2	0.900	0.841	0.075	0.984	3.812	0.208	−0.141	0.170	0.035	0.155	0.180	0.160	0.240
α	1.500	1.498	0.028	0.003	2.781	−0.025	−0.355	0.045	0.025	0.890	0.925	0.900	0.930

Notes: See notes to Table S.2.

Table S.6: Subsampling results (original parameterization) for $n = 50,000$ ($b = 1,357$, $N_b = 36$, $M = 200$)

									Quantile CI		Normal CI		
Parameter	True	Avg Est.	Std Est.	Dev. Mean	Dev. Std	Skew	Kurt	SW Rej.	JB Rej.	qCov90	qCov95	nCov90	nCov95
ρ_1	0.800	0.779	0.016	0.882	2.849	0.708	0.292	0.595	0.265	0.185	0.210	0.290	0.450
ρ_2	0.300	0.250	0.031	1.378	5.453	−0.192	−0.421	0.255	0.000	0.270	0.285	0.285	0.400
ς_1	0.700	0.782	0.065	−3.581	9.370	−0.828	0.112	0.820	0.285	0.170	0.175	0.170	0.245
ς_2	0.900	0.824	0.047	2.041	5.382	0.540	0.440	0.610	0.250	0.150	0.160	0.150	0.170
α	1.500	1.501	0.014	−0.035	2.805	−0.005	−0.244	0.055	0.025	0.870	0.915	0.850	0.920

Notes: See notes to Table S.2.

Table S.7: Subsampling results (original parameterization) for $n = 100{,}000$ ($b = 2{,}154$, $N_b = 46$, $M = 200$)

									Quantile CI		Normal CI		
Parameter	True	Avg Est.	Std Est.	Dev. Mean	Dev. Std	Skew	Kurt	SW Rej.	JB Rej.	qCov90	qCov95	nCov90	nCov95
ρ_1	0.800	0.778	0.013	1.104	2.944	0.889	0.849	0.770	0.635	0.155	0.155	0.145	0.175
ρ_2	0.300	0.249	0.025	1.750	5.651	−0.382	−0.019	0.360	0.050	0.175	0.210	0.170	0.200
ς_1	0.700	0.790	0.050	−4.298	10.040	−0.925	0.467	0.895	0.610	0.145	0.150	0.140	0.145
ς_2	0.900	0.819	0.040	2.816	5.924	0.666	0.639	0.860	0.460	0.140	0.145	0.135	0.140
α	1.500	1.501	0.009	−0.051	2.867	−0.004	−0.196	0.060	0.040	0.930	0.960	0.930	0.965

Notes: See notes to Table S.2.

approximation).

Table S.8: Subsampling results (reparameterized) for $n = 250$ ($b = 39$, $N_b = 6$, $M = 200$)

									Quantile CI		Normal CI		
Parameter	True	Avg Est.	Std Est.	Dev. Mean	Dev. Std	Skew	Kurt	SW Rej.	JB Rej.	qCov90	qCov95	nCov90	nCov95
ρ_1	0.800	0.782	0.128	−0.309	1.327	−0.518	−0.748	0.175	0.000	0.620	0.630	0.720	0.800
ρ_2	0.300	0.304	0.240	0.390	1.493	0.190	−0.931	0.230	0.000	0.270	0.290	0.350	0.430
σ	1.600	1.527	0.303	−0.146	3.038	0.134	−0.851	0.075	0.000	0.510	0.550	0.590	0.695
π_1	0.438	0.430	0.199	−0.092	1.258	0.044	−0.464	0.305	0.000	0.330	0.370	0.465	0.535
α	1.500	1.483	0.162	0.253	2.067	−0.107	−0.920	0.065	0.000	0.650	0.685	0.800	0.870

Notes: All results are in the reparameterized space $(\rho_1, \rho_2, \sigma, \pi_1, \alpha)$. SW and JB rejection rates are at the 5% level. qCov and nCov denote quantile-based and normal-approximation CI coverage. Confidence intervals are constructed from thinned overlapping blocks; normality diagnostics use non-overlapping blocks.

Table S.9: Subsampling results (reparameterized) for $n = 500$ ($b = 62$, $N_b = 8$, $M = 200$)

									Quantile CI		Normal CI		
Parameter	True	Avg Est.	Std Est.	Dev. Mean	Dev. Std	Skew	Kurt	SW Rej.	JB Rej.	qCov90	qCov95	nCov90	nCov95
ρ_1	0.800	0.804	0.111	−0.312	1.499	−0.565	−0.433	0.295	0.045	0.580	0.630	0.635	0.755
ρ_2	0.300	0.297	0.198	0.528	1.960	0.151	−0.762	0.315	0.020	0.385	0.400	0.525	0.575
σ	1.600	1.522	0.231	−0.333	3.273	0.220	−0.678	0.075	0.005	0.565	0.595	0.615	0.685
π_1	0.438	0.420	0.195	−0.201	1.621	−0.036	−0.238	0.375	0.080	0.300	0.320	0.500	0.575
α	1.500	1.489	0.113	0.209	2.404	−0.169	−0.780	0.075	0.000	0.765	0.800	0.855	0.915

Notes: See notes to Table S.8.

Table S.10: Subsampling results (reparameterized) for $n = 1,000$ ($b = 99$, $N_b = 10$, $M = 200$)

									Quantile CI		Normal CI		
Parameter	True	Avg Est.	Std Est.	Dev. Mean	Dev. Std	Skew	Kurt	SW Rej.	JB Rej.	qCov90	qCov95	nCov90	nCov95
ρ_1	0.800	0.812	0.086	−0.152	1.564	−0.415	−0.616	0.260	0.015	0.555	0.605	0.690	0.745
ρ_2	0.300	0.296	0.157	0.573	2.530	0.062	−0.963	0.300	0.010	0.450	0.455	0.595	0.660
σ	1.600	1.543	0.188	−0.545	3.759	0.190	−0.525	0.105	0.025	0.600	0.635	0.665	0.715
π_1	0.438	0.414	0.162	−0.467	2.010	−0.228	−0.420	0.380	0.070	0.285	0.315	0.510	0.610
α	1.500	1.493	0.093	0.128	2.493	−0.153	−0.586	0.045	0.010	0.800	0.815	0.825	0.885

Notes: See notes to Table S.8.

Table S.11: Subsampling results (reparameterized) for $n = 10,000$ ($b = 464$, $N_b = 21$, $M = 200$)

									Quantile CI		Normal CI		
Parameter	True	Avg Est.	Std Est.	Dev. Mean	Dev. Std	Skew	Kurt	SW Rej.	JB Rej.	qCov90	qCov95	nCov90	nCov95
ρ_1	0.800	0.786	0.029	0.427	2.386	0.177	−0.700	0.255	0.010	0.530	0.620	0.770	0.885
ρ_2	0.300	0.260	0.055	1.148	4.591	0.089	−0.973	0.265	0.000	0.505	0.520	0.705	0.825
σ	1.600	1.599	0.053	−1.377	5.329	0.008	−0.692	0.085	0.005	0.825	0.885	0.885	0.955
π_1	0.438	0.473	0.058	−1.554	3.897	−0.724	−0.437	0.735	0.070	0.210	0.230	0.490	0.735
α	1.500	1.498	0.028	0.003	2.781	−0.025	−0.355	0.045	0.025	0.895	0.925	0.900	0.940

Notes: See notes to Table S.8.

Table S.12: Subsampling results (reparameterized) for $n = 50,000$ ($b = 1,357$, $N_b = 36$, $M = 200$)

									Quantile CI		Normal CI		
Parameter	True	Avg Est.	Std Est.	Dev. Mean	Dev. Std	Skew	Kurt	SW Rej.	JB Rej.	qCov90	qCov95	nCov90	nCov95
ρ_1	0.800	0.779	0.016	0.882	2.849	0.708	0.292	0.595	0.265	0.190	0.205	0.305	0.450
ρ_2	0.300	0.250	0.031	1.378	5.453	−0.192	−0.421	0.255	0.000	0.270	0.280	0.305	0.415
σ	1.600	1.606	0.026	−1.540	5.833	−0.201	−0.429	0.030	0.005	0.825	0.875	0.900	0.940
π_1	0.438	0.487	0.035	−2.185	5.131	−1.158	0.980	0.965	0.720	0.175	0.180	0.155	0.190
α	1.500	1.501	0.014	−0.035	2.805	−0.005	−0.244	0.055	0.025	0.850	0.905	0.845	0.915

Notes: See notes to Table S.8.

Table S.13: Subsampling results (reparameterized) for $n = 100,000$ ($b = 2,154$, $N_b = 46$, $M = 200$)

									Quantile CI		Normal CI		
Parameter	True	Avg Est.	Std Est.	Dev. Mean	Dev. Std	Skew	Kurt	SW Rej.	JB Rej.	qCov90	qCov95	nCov90	nCov95
ρ_1	0.800	0.778	0.013	1.105	2.944	0.889	0.847	0.780	0.635	0.145	0.155	0.155	0.170
ρ_2	0.300	0.249	0.025	1.752	5.651	−0.382	−0.018	0.360	0.050	0.175	0.200	0.170	0.205
σ	1.600	1.609	0.017	−1.483	6.013	−0.305	−0.124	0.090	0.035	0.795	0.850	0.905	0.950
π_1	0.438	0.491	0.028	−2.593	5.455	−1.251	1.427	0.995	0.885	0.145	0.155	0.145	0.145
α	1.500	1.501	0.009	−0.051	2.867	−0.004	−0.196	0.060	0.040	0.910	0.960	0.925	0.965

Notes: See notes to Table S.8.

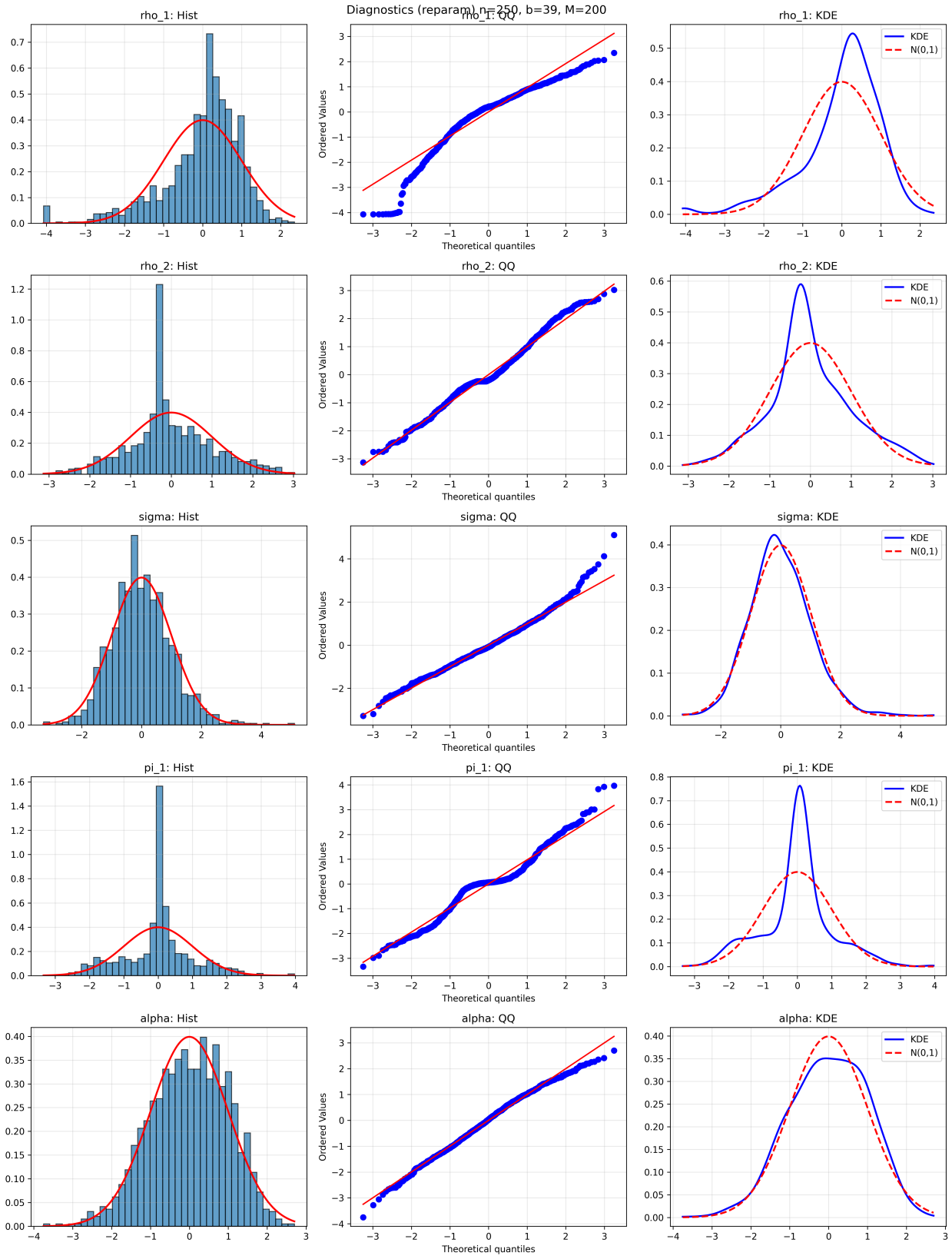

Figure S.7: Diagnostic plots for scaled subsample deviations (reparameterized) at $n = 250$. For each parameter (rows), we display: (left) histogram with standard normal overlay, (center) Q-Q plot against standard normal quantiles, and (right) kernel density estimate compared to the standard normal density. Deviations from the reference normal distribution are expected in small samples due to finite-sample effects.

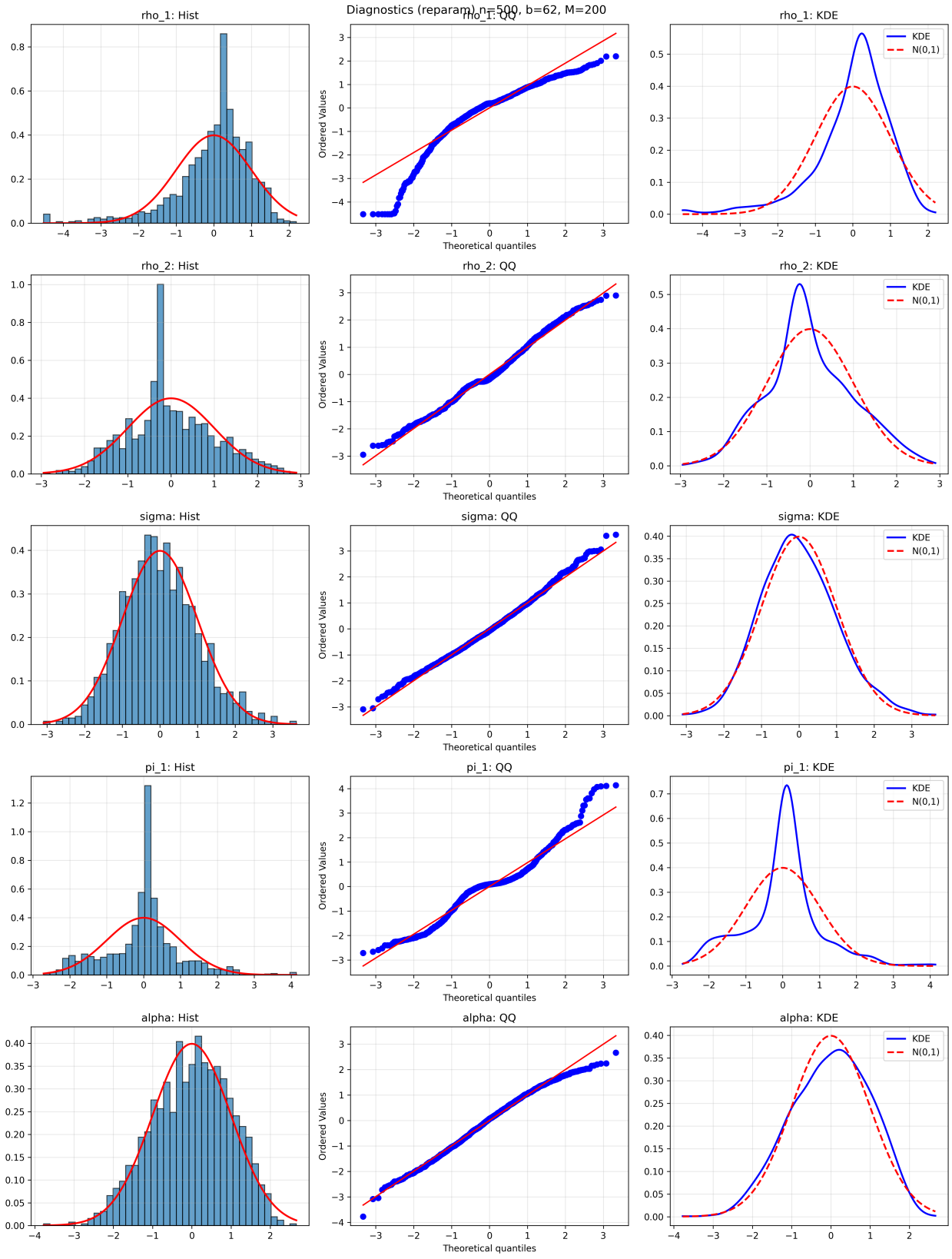

Figure S.8: Diagnostic plots for scaled subsample deviations (reparameterized) at $n = 500$. See caption to Figure S.7 for details.

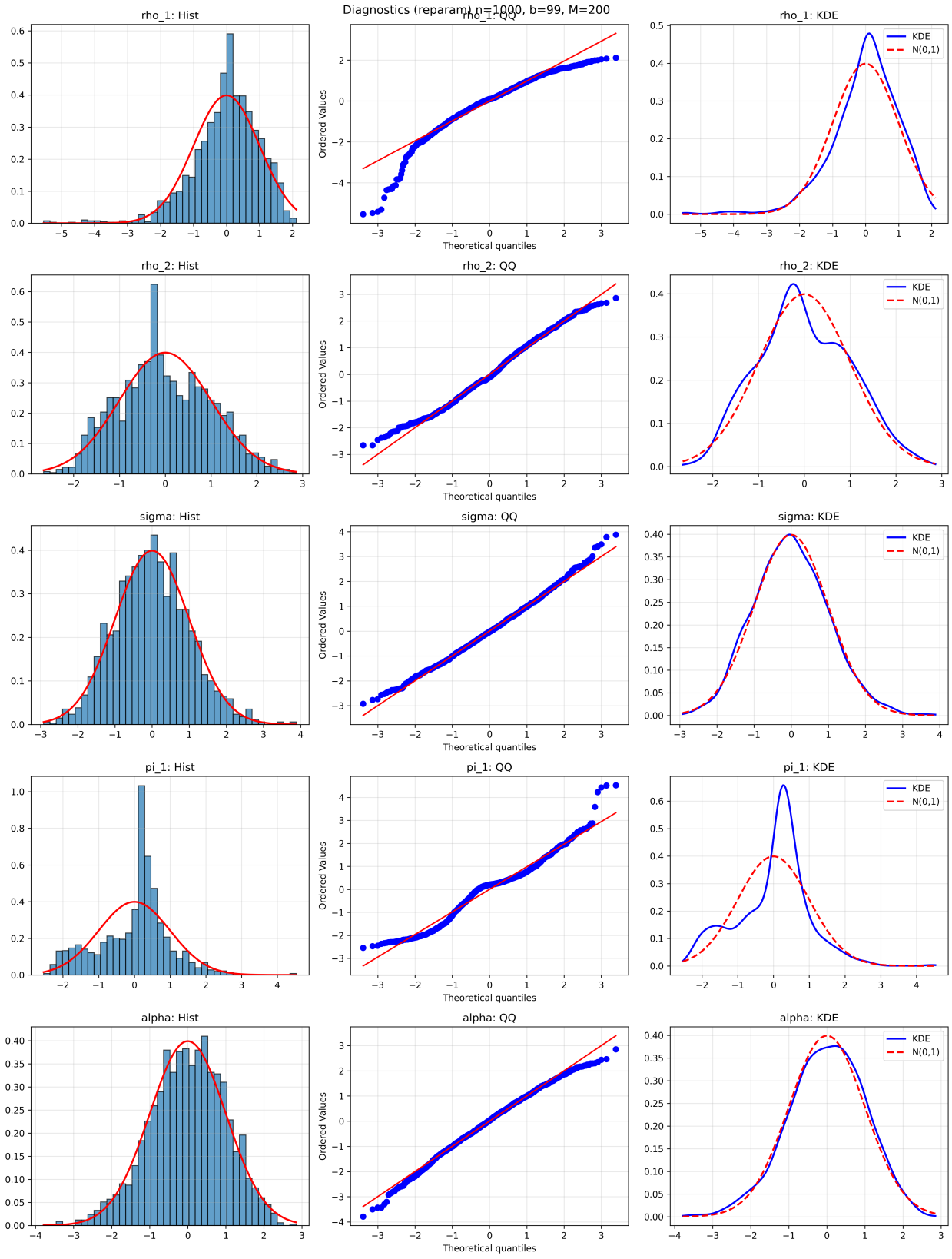

Figure S.9: Diagnostic plots for scaled subsample deviations (reparameterized) at $n = 1,000$. See caption to Figure S.7 for details.

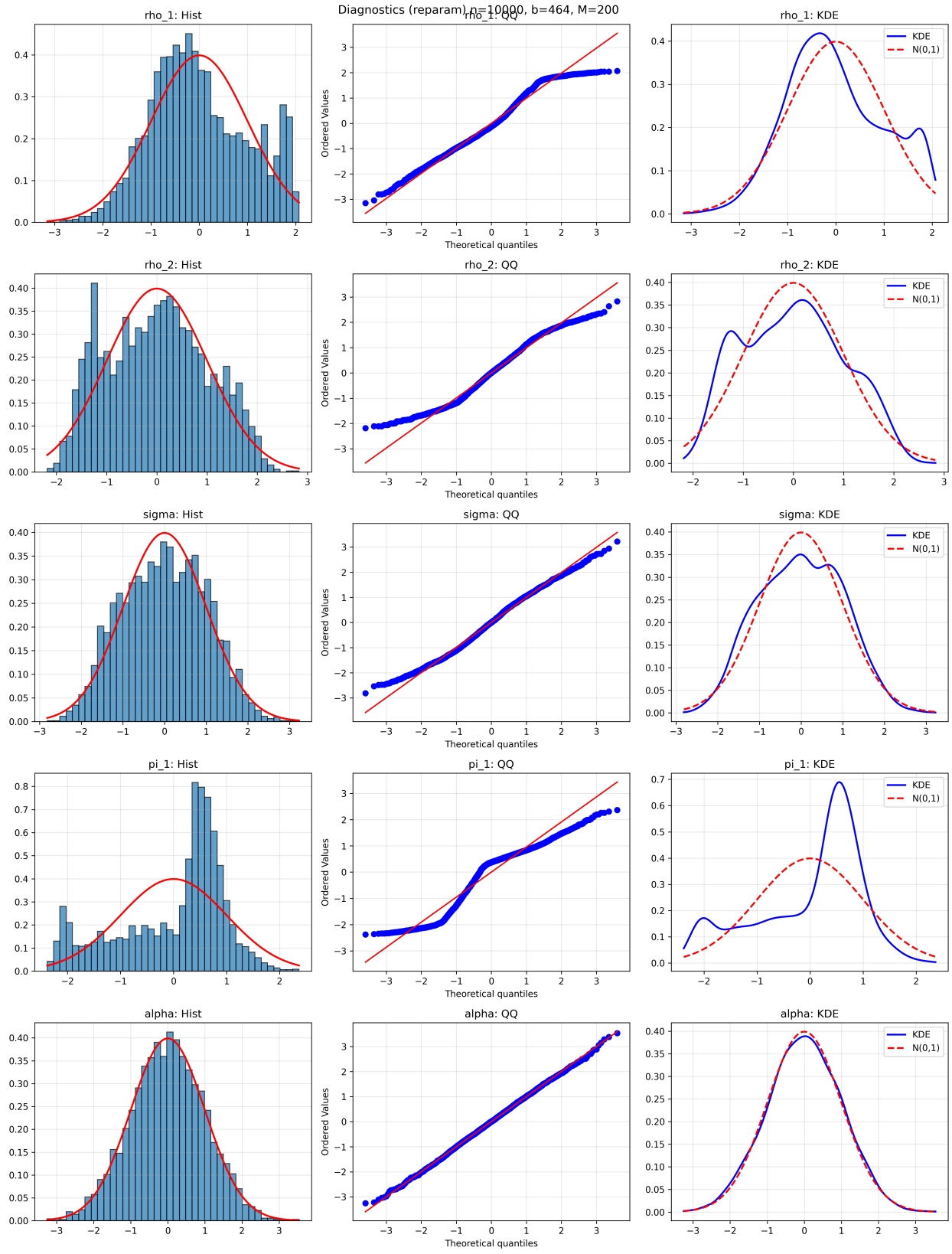

Figure S.10: Diagnostic plots for scaled subsample deviations (reparameterized) at $n = 10,000$. See caption to Figure S.7 for details.

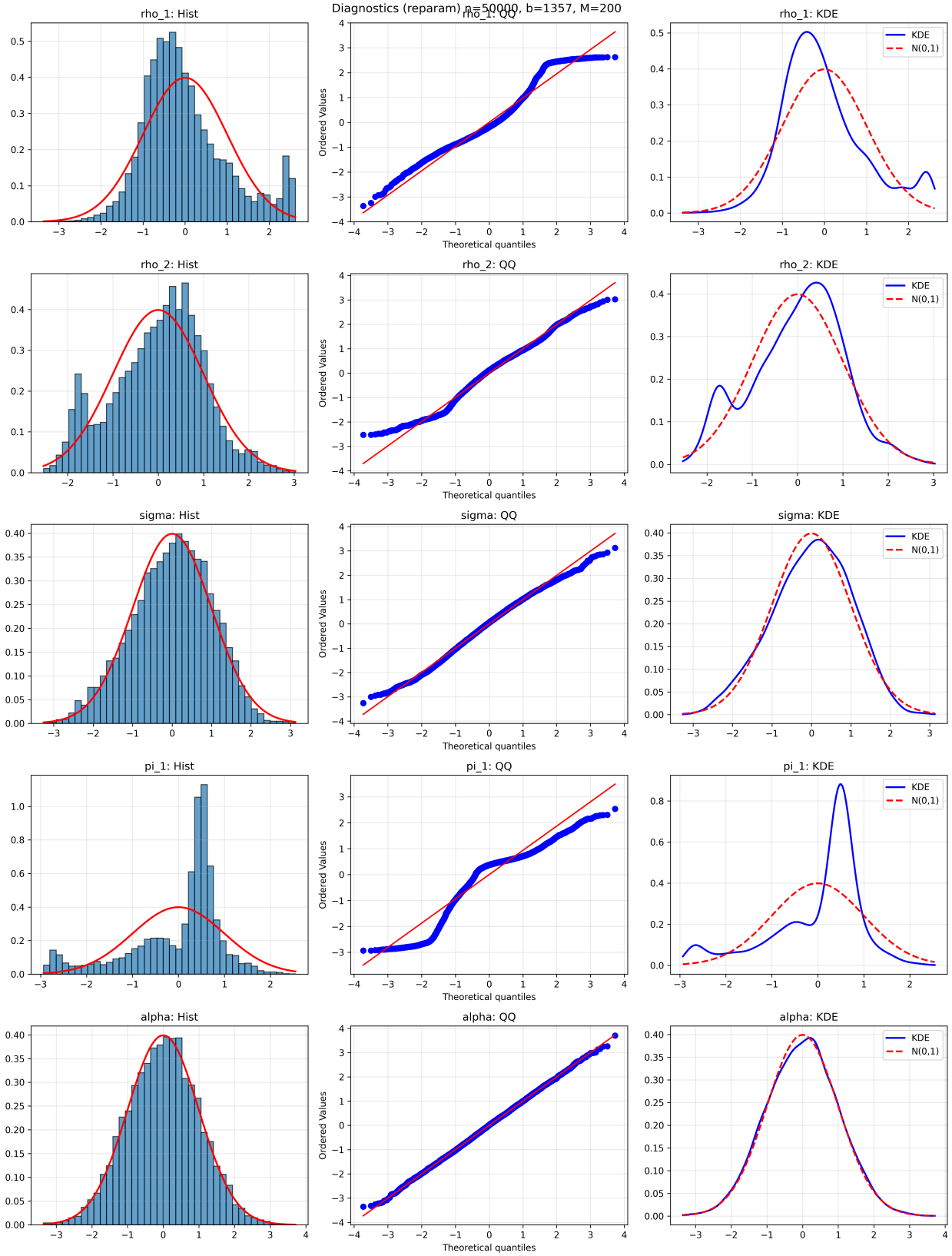

Figure S.11: Diagnostic plots for scaled subsample deviations (reparameterized) at $n = 50,000$. See caption to Figure S.7 for details.

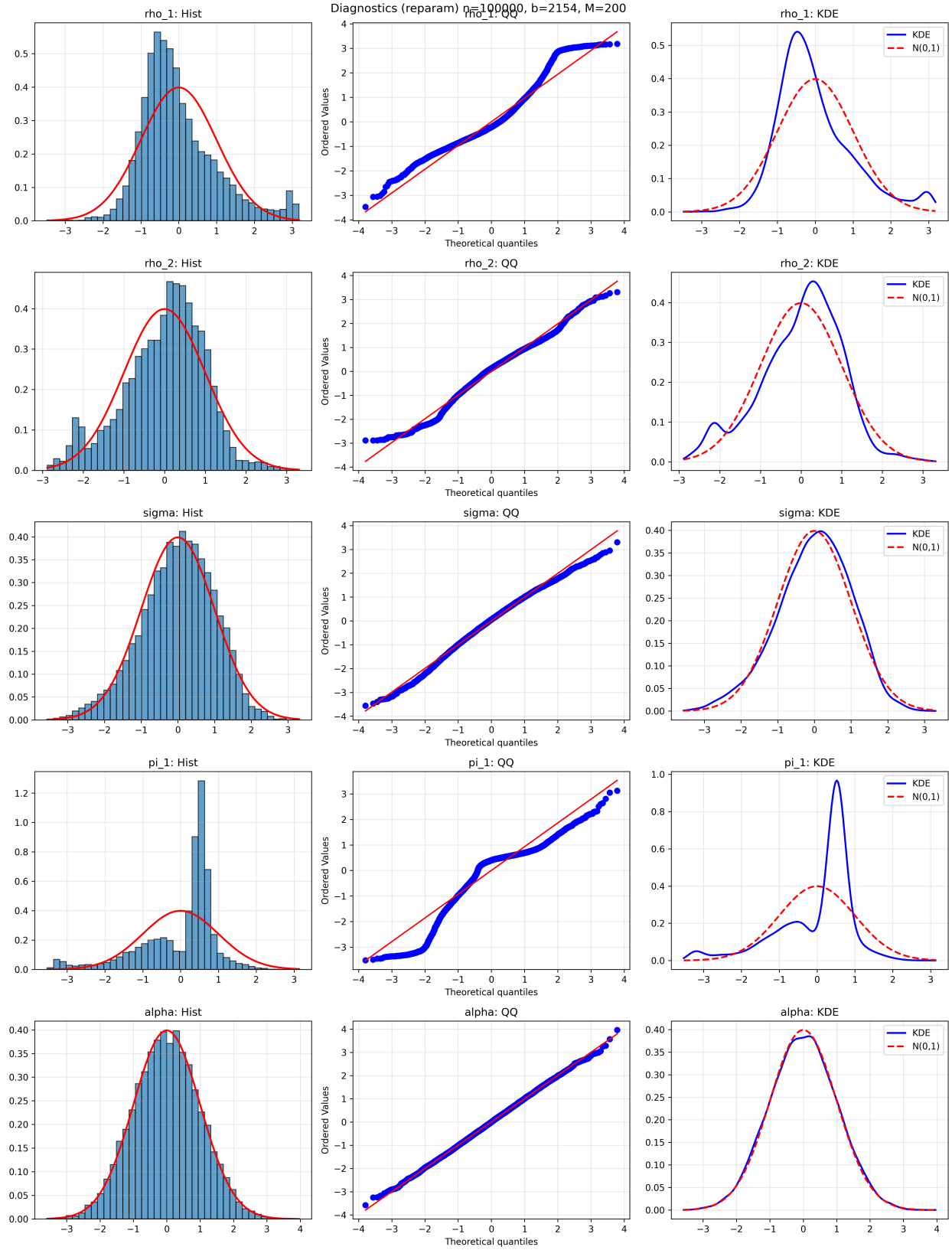

Figure S.12: Diagnostic plots for scaled subsample deviations (reparameterized) at $n = 100,000$. See caption to Figure S.7 for details. At this sample size, α and σ display near-perfect Gaussian alignment, while ρ_1, ρ_2, and π_1 retain visible departures consistent with the persistent finite-sample bias documented in Table S.13.

S.1.4. Criterion difference test for $H_0\colon \pi_1 = 1/2$

The poor identification of π_1 documented in Section S.1.3 raises the question of whether the mixing proportion is genuinely identified by the characteristic function-based objective. To address this formally, we implement a criterion difference test analogous to the classical likelihood ratio test in a GMM/MDE setting.

Let $\hat{\theta}_n^{\text{free}}$ denote the unrestricted MDE estimator (with π_1 free) and $\hat{\theta}_n^{\text{restr}}$ the restricted estimator imposing $\pi_1 = 1/2$ (i.e., $\varsigma_1 = \varsigma_2 = \sigma/2$). The criterion difference statistic is

$$\Delta_n = n\left[Q_n\left(\hat{\theta}_n^{\text{restr}}\right) - Q_n\left(\hat{\theta}_n^{\text{free}}\right)\right], \tag{S.4}$$

where $Q_n(\theta) = \int |\hat{\varphi}_n(s) - \varphi(s;\theta)|^2\, w(s)\, ds$ is the MDE objective function defined in equation (2.14) of the main paper. Under H_0 and standard regularity conditions, $\Delta_n \xrightarrow{d} \chi^2(1)$. Because the flatness of the objective surface may invalidate the χ^2 approximation, we supplement the asymptotic p-value with a subsampling-based p-value. For each non-overlapping subsample $\mathcal{X}_b^{(i)}$ of size $b = \lfloor n^{2/3} \rfloor$, we compute the subsample criterion difference $\Delta_b^{(i)} = b\left[Q_b^{(i)}\left(\hat{\theta}_b^{(i),\text{restr}}\right) - Q_b^{(i)}\left(\hat{\theta}_b^{(i),\text{free}}\right)\right]$ and define the subsampling p-value as

$$\hat{p}_{\text{sub}} = \frac{1}{N_b}\sum_{i=1}^{N_b} \mathbf{1}\left\{\Delta_b^{(i)} \geq \Delta_n\right\}. \tag{S.5}$$

We evaluate the test under the same DGP as in Sections S.1.2–S.1.3, with true parameter $\pi_1 = \varsigma_1/\sigma = 0.4375$. Since the true value is close to but not equal to $1/2$, the exercise simultaneously assesses the size of the χ^2 reference distribution and the power of the test to detect a moderate deviation from H_0. For each sample size $n \in \{500,\ 1{,}000,\ 10{,}000,\ 50{,}000\}$, we generate $M = 200$ Monte Carlo replications. Table S.14 reports the results.

Table S.14: Criterion difference test for $H_0\colon \pi_1 = 1/2$ (true $\pi_1 = 0.4375$, $M = 200$)

			Δ_n			Rejection rate	
n	b	M	Mean	Median	Std	$\chi^2(1)$ at 5%	Subsampling at 5%
500	62	200	0.006	0.001	0.011	0.000	0.105
1,000	99	200	0.007	0.001	0.014	0.000	0.090
10,000	464	200	0.007	0.000	0.015	0.000	0.105
50,000	1357	200	0.012	−0.001	0.029	0.000	0.175

Notes: $\Delta_n = n[Q_n(\hat{\theta}_n^{\text{restr}}) - Q_n(\hat{\theta}_n^{\text{free}})]$ is the criterion difference statistic defined in (S.4). The $\chi^2(1)$ column reports the fraction of replications for which the asymptotic p-value falls below 5%. The subsampling column reports the fraction for which $\hat{p}_{\text{sub}} < 0.05$. The subsample size is $b = \lfloor n^{2/3} \rfloor$.

The results in Table S.14 confirm that the MDE objective is essentially flat in the π_1 direction. The mean criterion difference Δ_n remains negligible across all sample sizes, and the asymptotic $\chi^2(1)$ test never rejects H_0 at the 5% level. The subsampling-based rejection rates hover around 10%, which is consistent

with the nominal size given the small number of non-overlapping blocks available at moderate sample sizes. Even at $n = 50{,}000$, the subsampling rejection rate of 17.5% remains modest, confirming that the departure from $\pi_1 = 1/2$ (the true value being 0.4375) is essentially undetectable by the CF-based objective. These findings motivate the restricted estimation strategy adopted in the next subsection.

S.1.5. Restricted subsampling under $\pi_1 = 1/2$

As discussed in the main text, the mixing proportion π_1 is the most difficult parameter to identify from the characteristic function-based objective. A criterion difference test for $H_0 \colon \pi_1 = 1/2$ confirms that the MDE objective is essentially flat in the π_1 direction, as the test never rejects H_0 at any conventional level for n up to $50,000$. Imposing $\pi_1 = 1/2$ reduces the parameter vector to $\theta_R = (\rho_1, \rho_2, \sigma, \alpha)$ and stabilizes inference on σ and α, which achieve near-nominal coverage at moderate sample sizes, at the cost of a small specification bias on (ρ_1, ρ_2) that becomes detectable at very large samples.

Table S.15: Restricted subsampling for $n = 250$ ($b = 39$, $M = 200$, $\pi_1 = 1/2$)

									Quantile CI		Normal CI		
Parameter	True	Avg Est.	Std Est.	Dev. Mean	Dev. Std	Skew	Kurt	SW Rej.	JB Rej.	qCov90	qCov95	nCov90	nCov95
ρ_1	0.800	0.713	0.116	−0.400	1.227	−0.470	−0.709	0.120	0.000	0.730	0.785	0.715	0.780
ρ_2	0.300	0.299	0.258	0.415	1.592	0.215	−0.866	0.290	0.000	0.225	0.225	0.320	0.380
σ	1.600	1.612	0.269	0.190	2.953	0.108	−0.868	0.070	0.000	0.590	0.670	0.695	0.770
α	1.500	1.492	0.157	0.309	1.993	−0.081	−0.935	0.090	0.000	0.640	0.680	0.795	0.865

Notes: See notes to Table S.8. Estimation under the restriction $\varsigma_1 = \varsigma_2 = \sigma/2$.

Table S.16: Restricted subsampling for $n = 500$ ($b = 62$, $M = 200$, $\pi_1 = 1/2$)

									Quantile CI		Normal CI		
Parameter	True	Avg Est.	Std Est.	Dev. Mean	Dev. Std	Skew	Kurt	SW Rej.	JB Rej.	qCov90	qCov95	nCov90	nCov95
ρ_1	0.800	0.728	0.118	−0.457	1.312	−0.535	−0.324	0.205	0.035	0.770	0.800	0.755	0.805
ρ_2	0.300	0.295	0.236	0.539	2.073	0.163	−0.756	0.420	0.035	0.295	0.305	0.415	0.460
σ	1.600	1.604	0.181	0.175	3.100	0.084	−0.667	0.045	0.000	0.675	0.750	0.750	0.845
α	1.500	1.497	0.109	0.289	2.323	−0.161	−0.774	0.075	0.000	0.795	0.815	0.865	0.910

Notes: See notes to Table S.15.

Table S.17: Restricted subsampling for $n = 1,000$ ($b = 99$, $M = 200$, $\pi_1 = 1/2$)

									Quantile CI		Normal CI		
Parameter	True	Avg Est.	Std Est.	Dev. Mean	Dev. Std	Skew	Kurt	SW Rej.	JB Rej.	qCov90	qCov95	nCov90	nCov95
ρ_1	0.800	0.747	0.099	−0.468	1.262	−0.491	−0.361	0.160	0.045	0.870	0.890	0.800	0.870
ρ_2	0.300	0.270	0.198	0.700	2.644	0.132	−1.028	0.550	0.025	0.320	0.325	0.475	0.580
σ	1.600	1.606	0.146	0.200	3.425	0.092	−0.458	0.055	0.010	0.695	0.745	0.755	0.820
α	1.500	1.498	0.089	0.236	2.401	−0.107	−0.596	0.045	0.010	0.800	0.810	0.830	0.885

Notes: See notes to Table S.15.

Table S.18: Restricted subsampling for $n = 10,000$ ($b = 464$, $M = 200$, $\pi_1 = 1/2$)

									Quantile CI		Normal CI		
Parameter	True	Avg Est.	Std Est.	Dev. Mean	Dev. Std	Skew	Kurt	SW Rej.	JB Rej.	qCov90	qCov95	nCov90	nCov95
ρ_1	0.800	0.773	0.011	−0.540	1.287	−0.551	0.045	0.185	0.095	0.560	0.715	0.270	0.425
ρ_2	0.300	0.239	0.056	0.873	4.877	0.332	−1.038	0.575	0.005	0.400	0.400	0.625	0.725
σ	1.600	1.609	0.044	0.242	4.153	0.166	−0.400	0.045	0.005	0.855	0.895	0.865	0.905
α	1.500	1.499	0.027	0.157	2.669	0.014	−0.361	0.050	0.020	0.890	0.915	0.895	0.925

Notes: See notes to Table S.15.

Table S.19: Restricted subsampling for $n = 50,000$ ($b = 1,357$, $M = 200$, $\pi_1 = 1/2$)

									Quantile CI		Normal CI		
Parameter	True	Avg Est.	Std Est.	Dev. Mean	Dev. Std	Skew	Kurt	SW Rej.	JB Rej.	qCov90	qCov95	nCov90	nCov95
ρ_1	0.800	0.774	0.005	−0.322	1.257	−0.632	0.814	0.335	0.320	0.000	0.015	0.000	0.000
ρ_2	0.300	0.238	0.026	0.488	5.779	0.231	−0.572	0.255	0.000	0.185	0.185	0.215	0.360
σ	1.600	1.609	0.021	0.142	4.434	0.146	−0.355	0.045	0.030	0.865	0.915	0.850	0.920
α	1.500	1.501	0.013	0.099	2.727	0.011	−0.243	0.055	0.025	0.875	0.915	0.870	0.925

Notes: See notes to Table S.15.

Table S.20: Restricted subsampling for $n = 100,000$ ($b = 2,154$, $M = 200$, $\pi_1 = 1/2$)

									Quantile CI		Normal CI		
Parameter	True	Avg Est.	Std Est.	Dev. Mean	Dev. Std	Skew	Kurt	SW Rej.	JB Rej.	qCov90	qCov95	nCov90	nCov95
ρ_1	0.800	0.774	0.003	−0.248	1.197	−0.534	0.786	0.275	0.290	0.000	0.000	0.000	0.000
ρ_2	0.300	0.240	0.018	0.353	6.069	0.087	−0.369	0.090	0.000	0.075	0.115	0.065	0.120
σ	1.600	1.610	0.014	0.113	4.609	0.090	−0.278	0.050	0.010	0.840	0.905	0.835	0.900
α	1.500	1.501	0.008	0.080	2.788	0.013	−0.199	0.065	0.040	0.935	0.955	0.940	0.975

Notes: See notes to Table S.15.

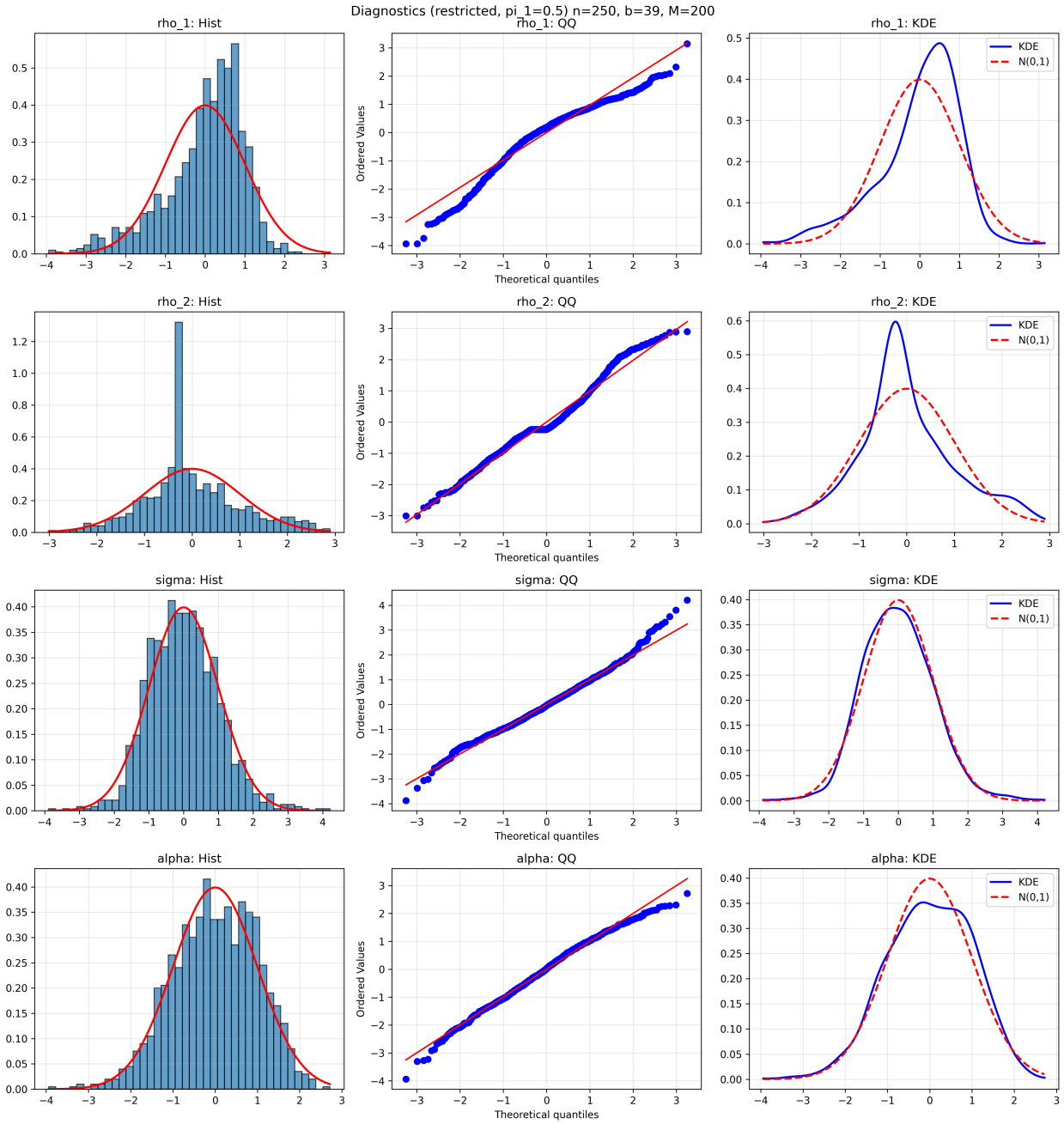

Figure S.13: Diagnostic plots for restricted subsampling ($\pi_1 = 1/2$) at $n = 250$. For each parameter (rows): histogram with standard normal overlay (left), Q-Q plot (center), and kernel density estimate vs. $\mathcal{N}(0, 1)$ (right).

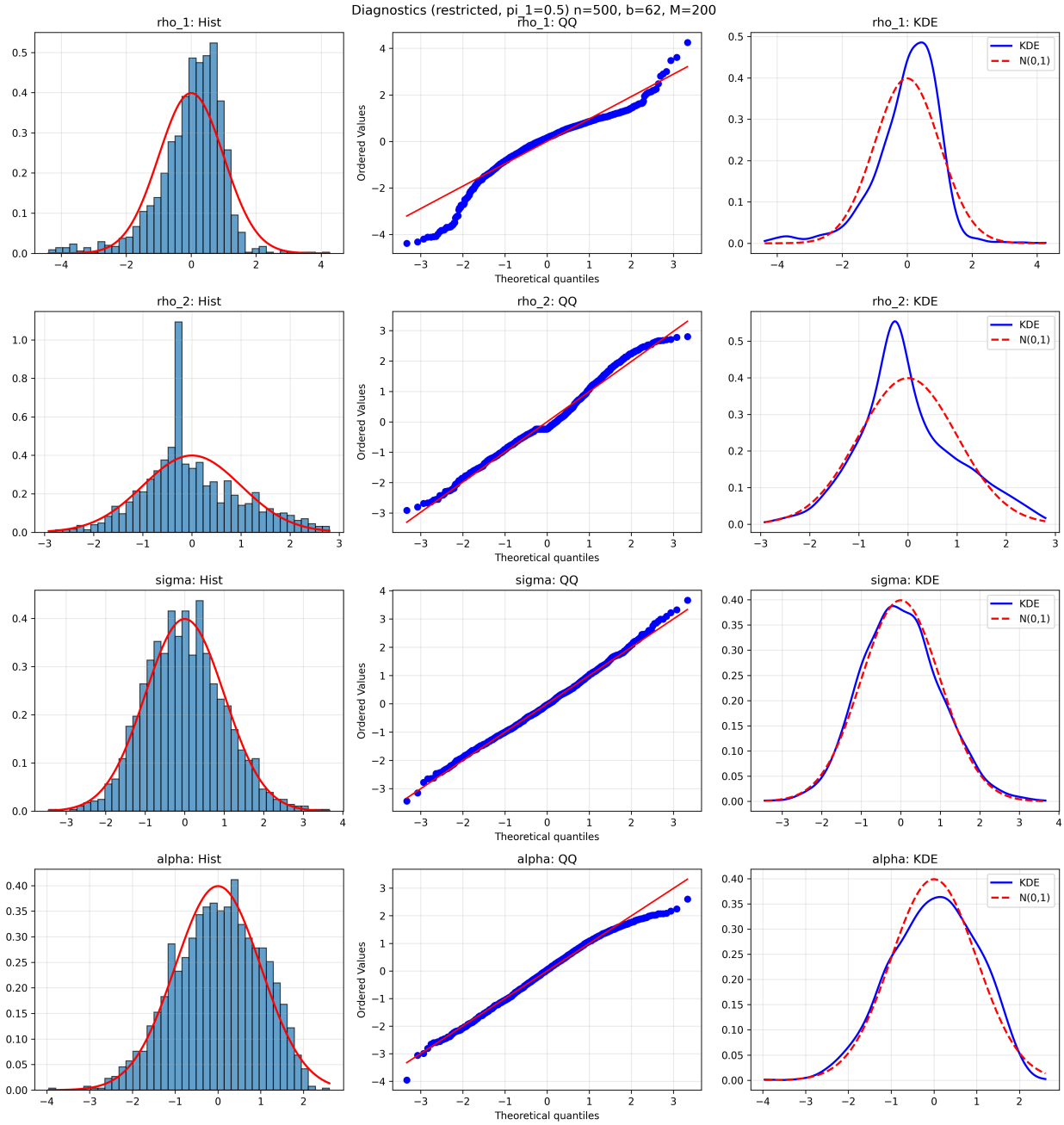

Figure S.14: Diagnostic plots for restricted subsampling ($\pi_1 = 1/2$) at $n = 500$. See caption to Figure S.13 for details.

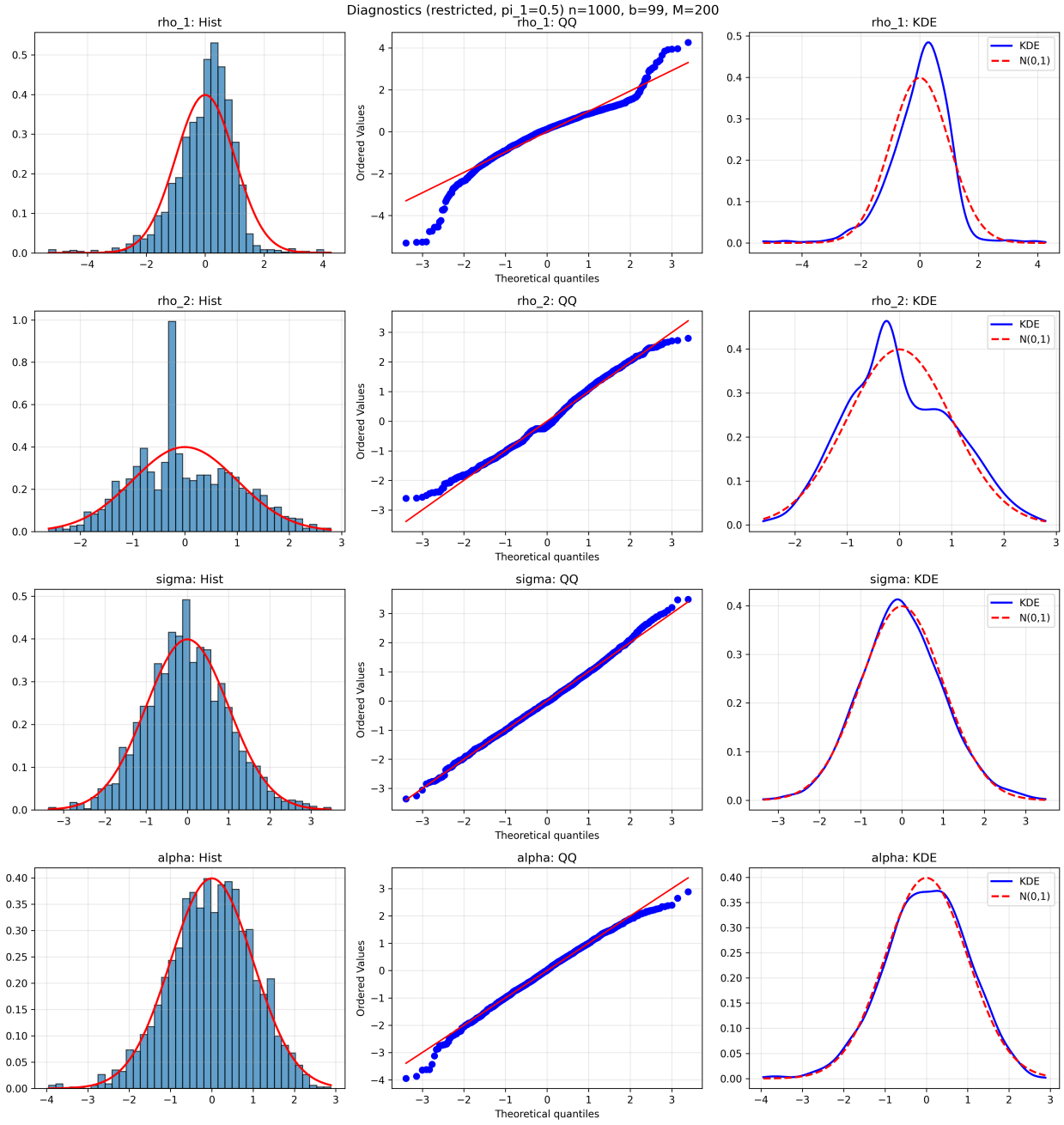

Figure S.15: Diagnostic plots for restricted subsampling ($\pi_1 = 1/2$) at $n = 1,000$. See caption to Figure S.13 for details.

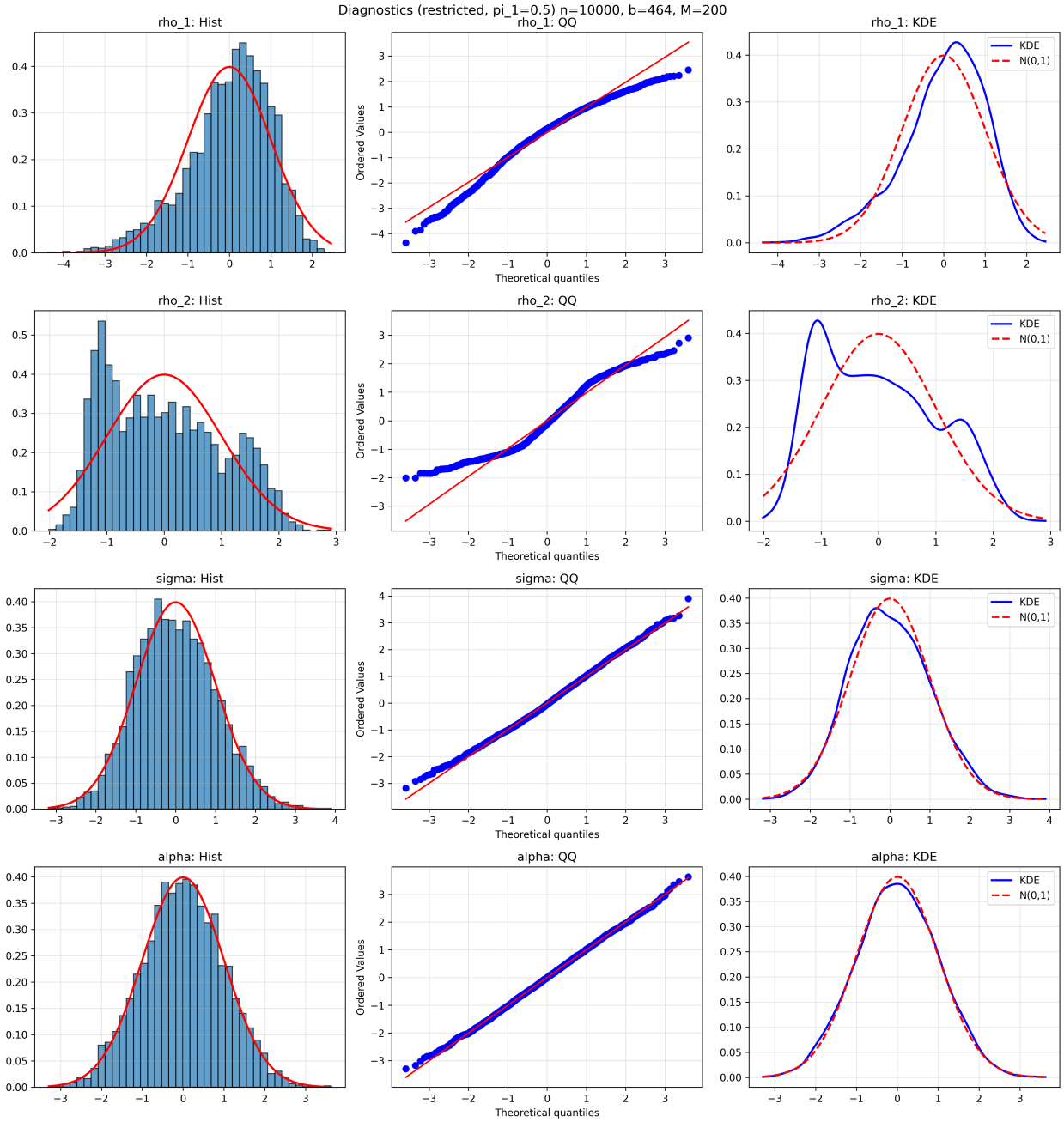

Figure S.16: Diagnostic plots for restricted subsampling ($\pi_1 = 1/2$) at $n = 10,000$. See caption to Figure S.13 for details.

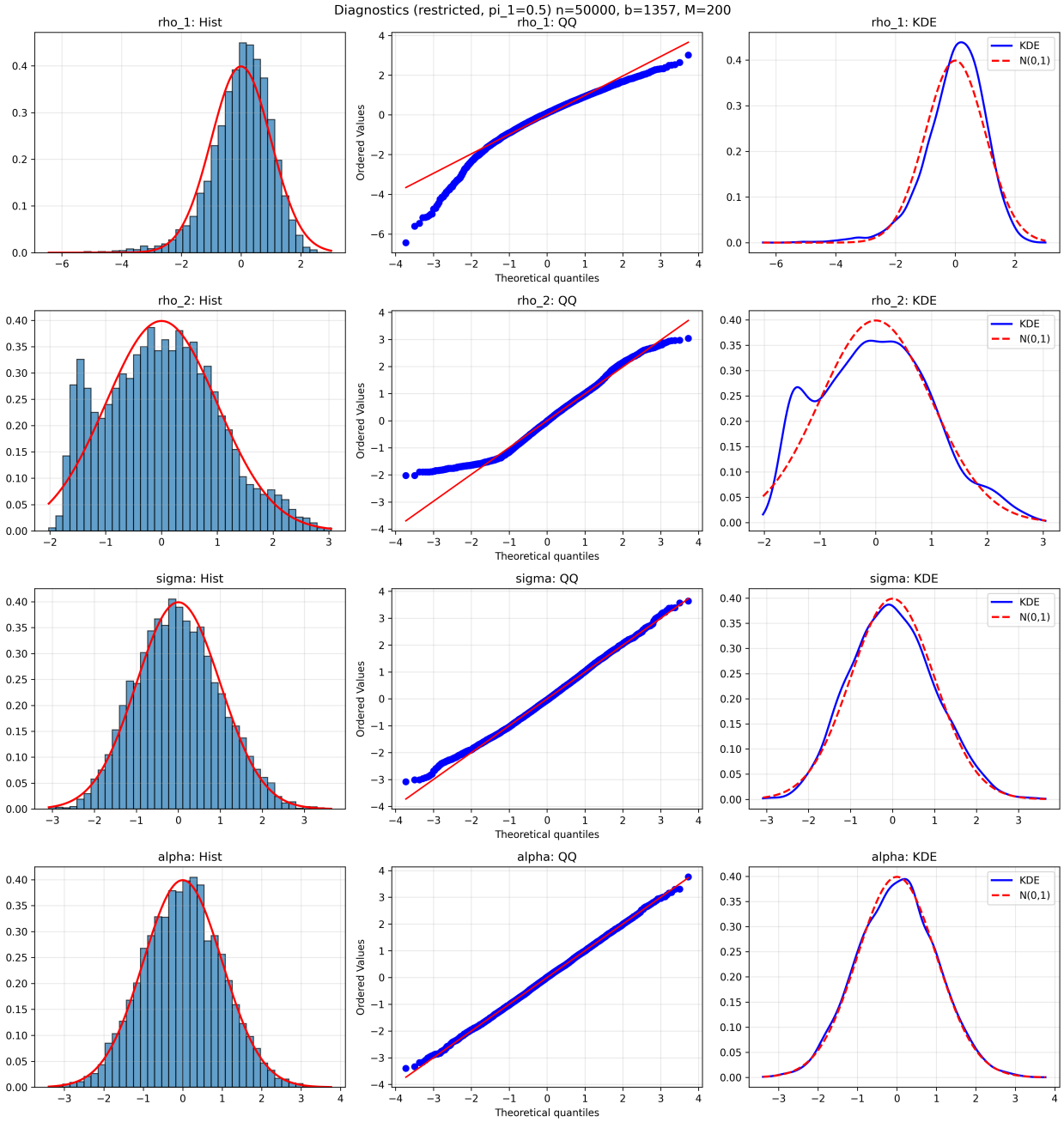

Figure S.17: Diagnostic plots for restricted subsampling ($\pi_1 = 1/2$) at $n = 50,000$. See caption to Figure S.13 for details.

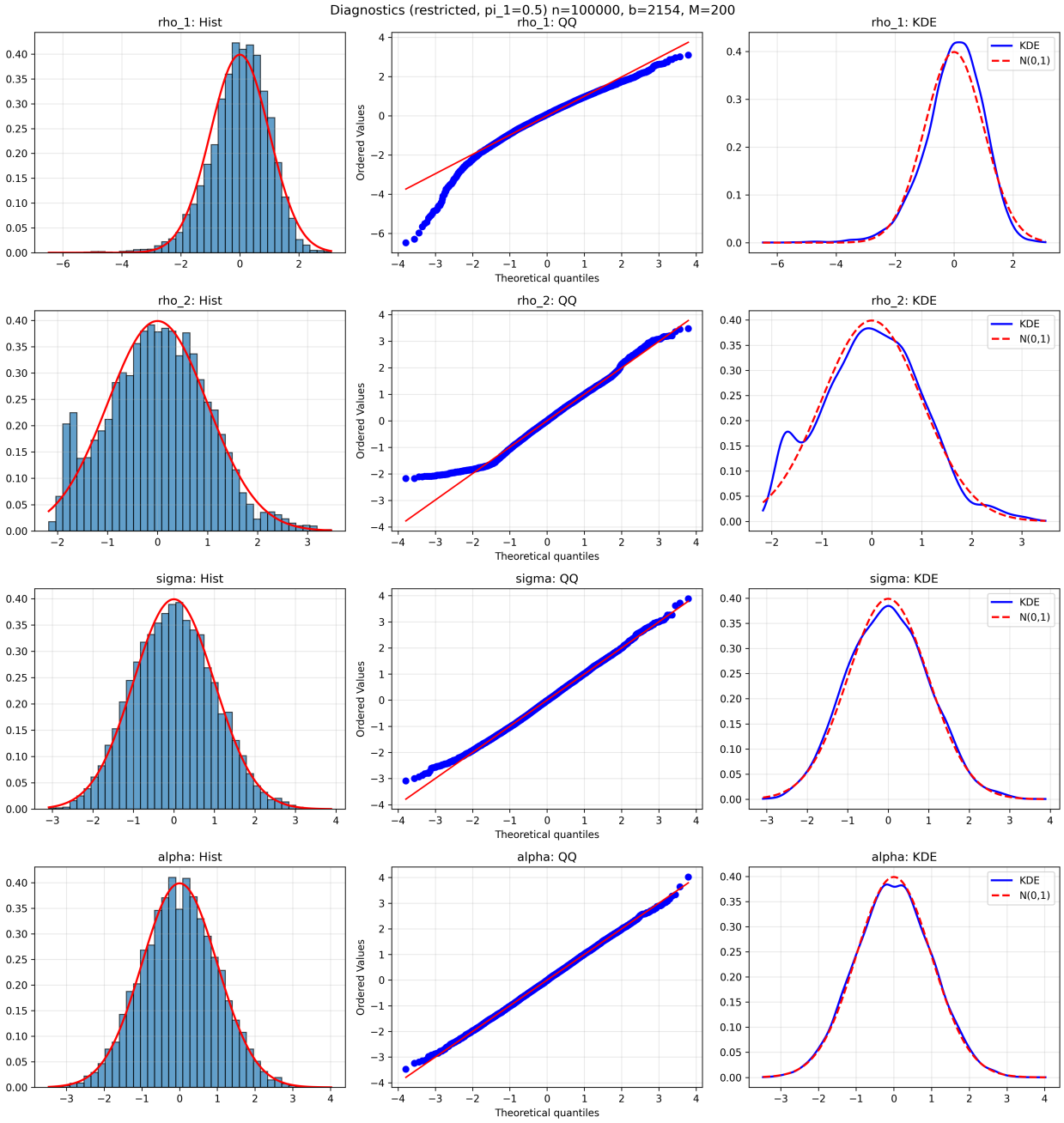

Figure S.18: Diagnostic plots for restricted subsampling ($\pi_1 = 1/2$) at $n = 100,000$. See caption to Figure S.13 for details. At this sample size, σ and α display near-perfect Gaussian alignment, while ρ_1 retains visible left skewness and a heavy left tail consistent with the specification bias induced by the constraint $\pi_1 = 1/2 \neq 0.4375$.

S.1.6. Restricted subsampling under $\pi_1 = 0.4375$ (true value)

Section S.1.5 imposed the (false) restriction $\pi_1 = 1/2$ to assess the trade-off between specification bias and estimation stability. We now complement that analysis by imposing the *true* restriction $\pi_1 = \pi_{1,0} = 0.4375$, so that the restricted parameter vector becomes $\theta_R = (\rho_1, \rho_2, \sigma, \alpha)$ under a correctly specified constraint. Since the restriction is now compatible with the data-generating process, this exercise provides a benchmark: any remaining finite-sample distortions in coverage or normality are attributable solely to the slow convergence of the subsampling approximation, not to specification bias.

Tables S.21–S.26 report the subsampling diagnostics for $n \in \{250,\ 500,\ 1,000,\ 10,000,\ 50,000\ 100,000\}$, and Figures S.19–S.24 display the corresponding graphical diagnostics.

Table S.21: Restricted subsampling for $n = 250$ ($b = 39$, $M = 200$, $\pi_1 = 0.4375$)

									Quantile CI		Normal CI		
Parameter	True	Avg Est.	Std Est.	Dev. Mean	Dev. Std	Skew	Kurt	SW Rej.	JB Rej.	qCov90	qCov95	nCov90	nCov95
ρ_1	0.800	0.730	0.138	−0.411	1.226	−0.434	−0.734	0.130	0.000	0.640	0.695	0.715	0.790
ρ_2	0.300	0.327	0.249	0.280	1.660	0.121	−0.898	0.250	0.000	0.205	0.220	0.360	0.430
σ	1.600	1.594	0.276	0.151	2.936	0.095	−0.863	0.060	0.000	0.570	0.635	0.685	0.775
α	1.500	1.489	0.158	0.302	2.005	−0.078	−0.938	0.090	0.000	0.640	0.685	0.790	0.870

Notes: All results are in the reparameterized space $(\rho_1, \rho_2, \sigma, \alpha)$ under the true restriction $\pi_1 = 0.4375$. SW and JB rejection rates are at the 5% level. qCov and nCov denote quantile-based and normal-approximation CI coverage. Confidence intervals are constructed from thinned overlapping blocks; normality diagnostics use non-overlapping blocks.

Table S.22: Restricted subsampling for $n = 500$ ($b = 62$, $M = 200$, $\pi_1 = 0.4375$)

									Quantile CI		Normal CI		
Parameter	True	Avg Est.	Std Est.	Dev. Mean	Dev. Std	Skew	Kurt	SW Rej.	JB Rej.	qCov90	qCov95	nCov90	nCov95
ρ_1	0.800	0.751	0.130	−0.469	1.313	−0.576	−0.329	0.185	0.035	0.690	0.750	0.805	0.835
ρ_2	0.300	0.329	0.217	0.317	2.099	0.120	−0.807	0.375	0.035	0.295	0.315	0.475	0.540
σ	1.600	1.590	0.185	0.116	3.098	0.083	−0.671	0.045	0.000	0.660	0.720	0.740	0.820
α	1.500	1.494	0.110	0.283	2.337	−0.156	−0.787	0.070	0.000	0.780	0.810	0.860	0.910

Notes: See notes to Table S.21.

Table S.23: Restricted subsampling for $n = 1,000$ ($b = 99$, $M = 200$, $\pi_1 = 0.4375$)

									Quantile CI		Normal CI		
Parameter	True	Avg Est.	Std Est.	Dev. Mean	Dev. Std	Skew	Kurt	SW Rej.	JB Rej.	qCov90	qCov95	nCov90	nCov95
ρ_1	0.800	0.761	0.131	−0.513	1.324	−0.491	−0.344	0.170	0.060	0.750	0.780	0.860	0.885
ρ_2	0.300	0.321	0.190	0.424	2.583	0.052	−1.075	0.405	0.010	0.370	0.375	0.510	0.595
σ	1.600	1.594	0.151	0.124	3.438	0.092	−0.466	0.070	0.010	0.680	0.740	0.750	0.810
α	1.500	1.496	0.090	0.222	2.410	−0.108	−0.607	0.045	0.010	0.800	0.820	0.825	0.880

Notes: See notes to Table S.21.

Table S.24: Restricted subsampling for $n = 10,000$ ($b = 464$, $M = 200$, $\pi_1 = 0.4375$)

									Quantile CI		Normal CI		
Parameter	True	Avg Est.	Std Est.	Dev. Mean	Dev. Std	Skew	Kurt	SW Rej.	JB Rej.	qCov90	qCov95	nCov90	nCov95
ρ_1	0.800	0.799	0.010	−0.599	1.412	−0.704	0.191	0.295	0.165	0.890	0.920	0.965	0.980
ρ_2	0.300	0.298	0.050	0.369	4.693	0.131	−1.036	0.280	0.000	0.775	0.775	0.865	0.920
σ	1.600	1.599	0.044	0.093	4.287	0.141	−0.437	0.045	0.010	0.830	0.880	0.860	0.925
α	1.500	1.498	0.028	0.123	2.707	0.006	−0.359	0.050	0.020	0.880	0.915	0.895	0.925

Notes: See notes to Table S.21.

Table S.25: Restricted subsampling for $n = 50{,}000$ ($b = 1{,}357$, $M = 200$, $\pi_1 = 0.4375$)

									Quantile CI		Normal CI		
Parameter	True	Avg Est.	Std Est.	Dev. Mean	Dev. Std	Skew	Kurt	SW Rej.	JB Rej.	qCov90	qCov95	nCov90	nCov95
ρ_1	0.800	0.799	0.005	−0.341	1.342	−0.819	1.190	0.435	0.390	0.905	0.925	0.935	0.965
ρ_2	0.300	0.298	0.025	0.104	5.371	0.055	−0.410	0.045	0.005	0.910	0.940	0.875	0.935
σ	1.600	1.600	0.022	0.019	4.541	0.119	−0.351	0.030	0.020	0.875	0.920	0.890	0.920
α	1.500	1.500	0.013	0.066	2.763	0.007	−0.242	0.055	0.025	0.870	0.915	0.860	0.905

Notes: See notes to Table S.21.

Table S.26: Restricted subsampling for $n = 100{,}000$ ($b = 2{,}154$, $M = 200$, $\pi_1 = 0.4375$)

									Quantile CI		Normal CI		
Parameter	True	Avg Est.	Std Est.	Dev. Mean	Dev. Std	Skew	Kurt	SW Rej.	JB Rej.	qCov90	qCov95	nCov90	nCov95
ρ_1	0.800	0.800	0.003	−0.254	1.257	−0.768	1.430	0.445	0.405	0.920	0.955	0.950	0.980
ρ_2	0.300	0.301	0.017	0.043	5.484	−0.011	−0.107	0.030	0.005	0.925	0.975	0.900	0.980
σ	1.600	1.601	0.014	0.019	4.677	0.072	−0.211	0.040	0.015	0.885	0.935	0.895	0.945
α	1.500	1.500	0.008	0.056	2.822	0.010	−0.191	0.065	0.040	0.920	0.960	0.940	0.965

Notes: See notes to Table S.21.

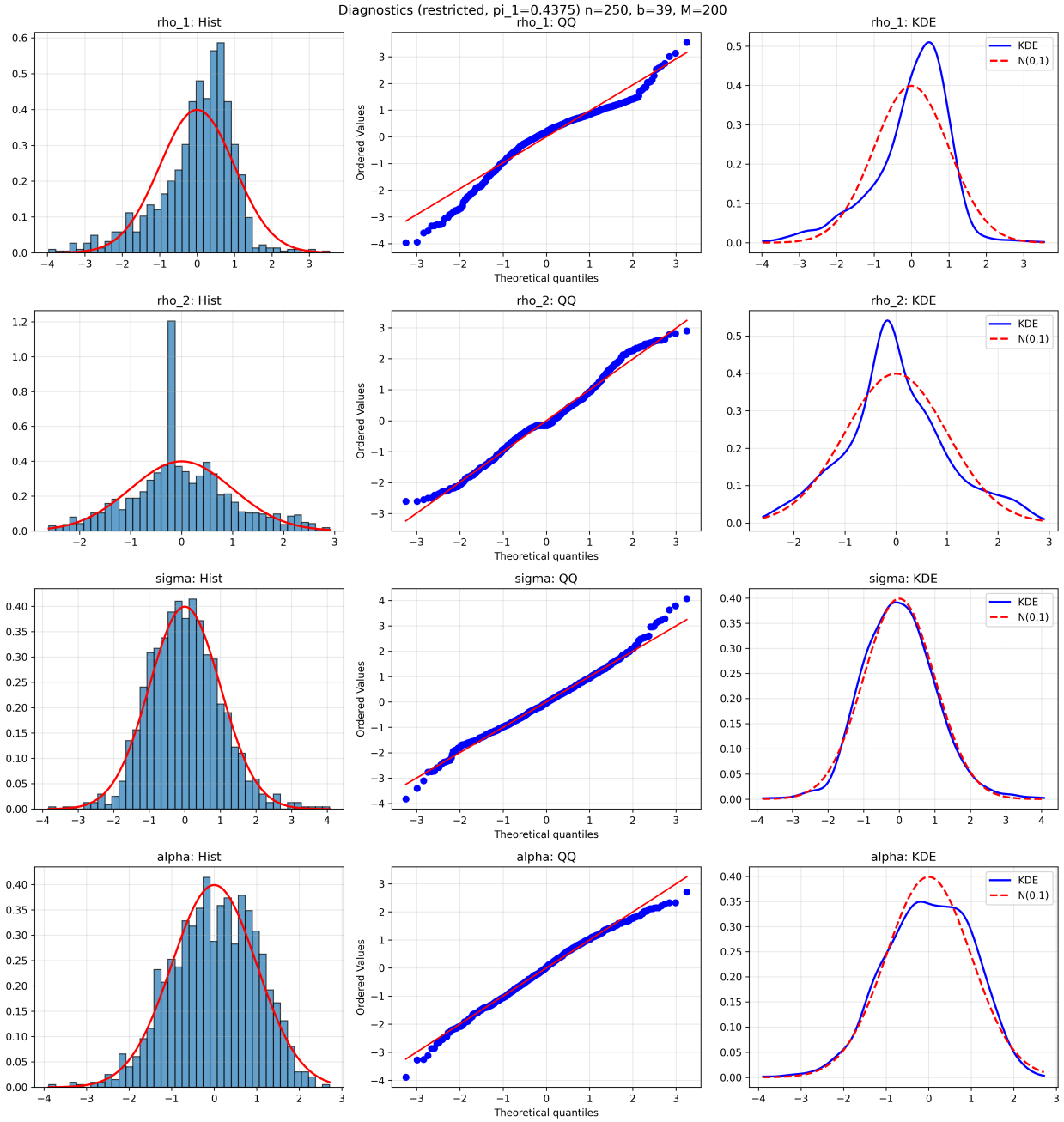

Figure S.19: Diagnostic plots for restricted subsampling ($\pi_1 = 0.4375$) at $n = 250$. For each parameter (rows): histogram with standard normal overlay (left), Q-Q plot (center), and kernel density estimate vs. $\mathcal{N}(0, 1)$ (right).

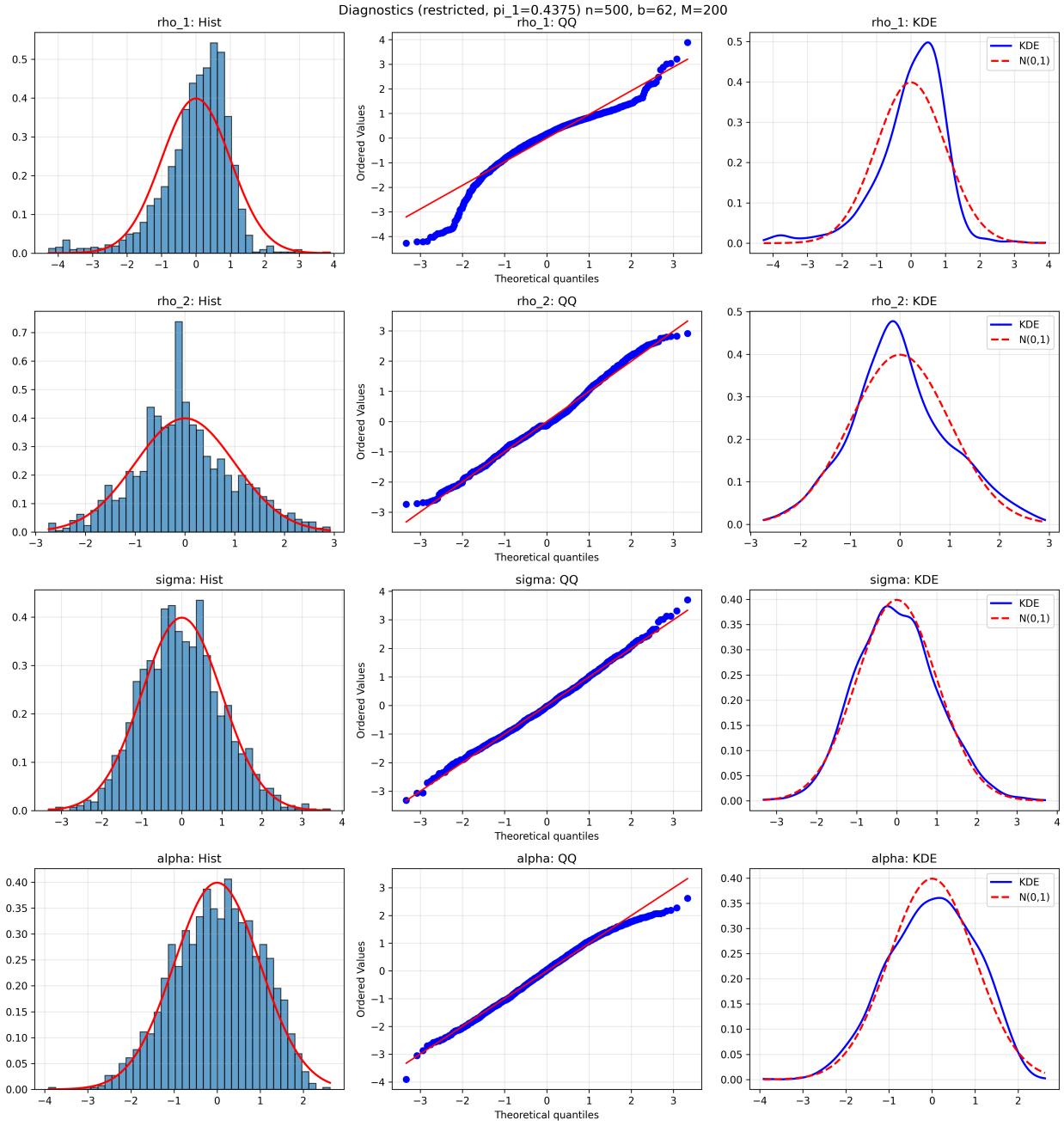

Figure S.20: Diagnostic plots for restricted subsampling ($\pi_1 = 0.4375$) at $n = 500$. See caption to Figure S.19 for details.

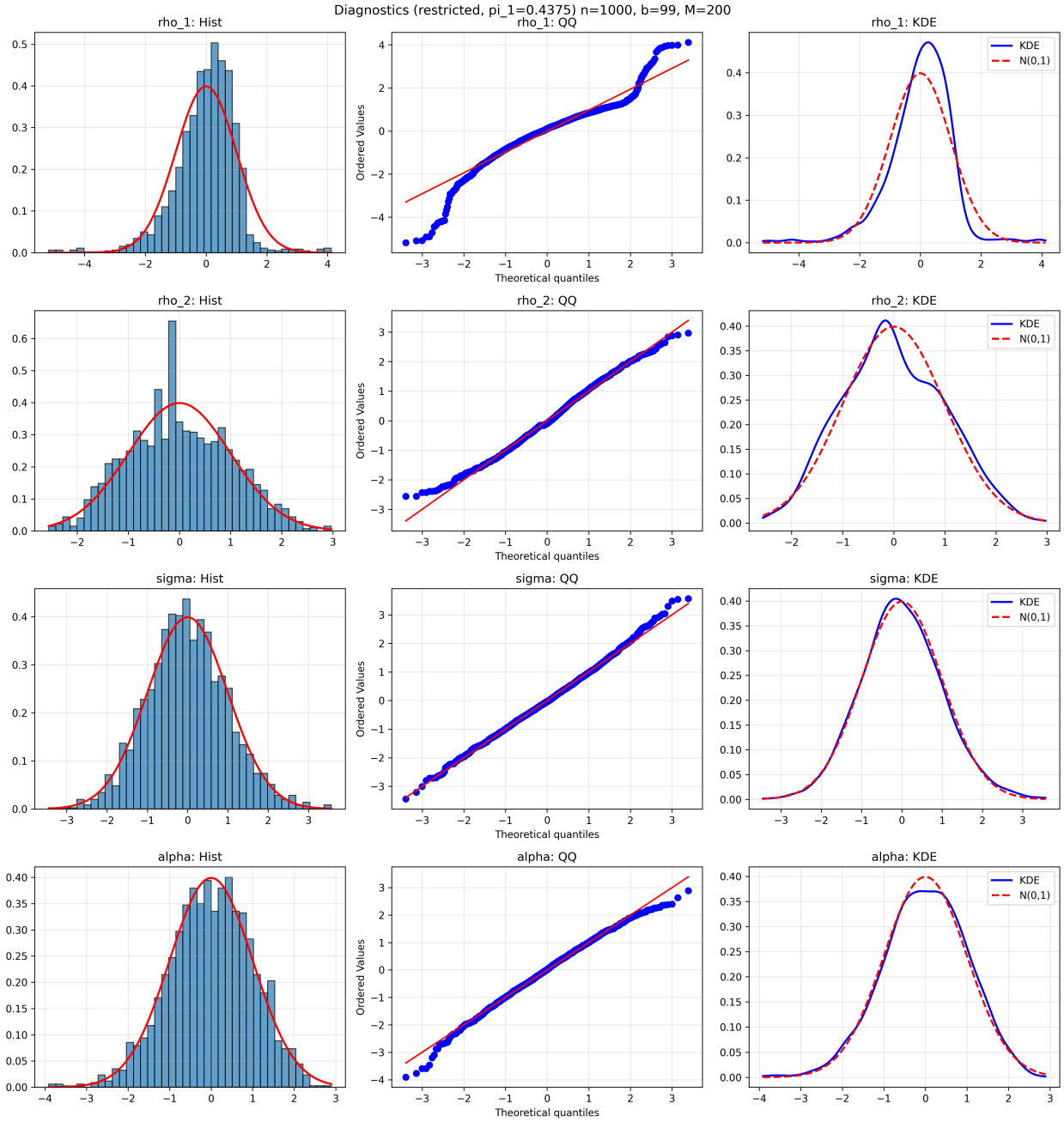

Figure S.21: Diagnostic plots for restricted subsampling ($\pi_1 = 0.4375$) at $n = 1,000$. See caption to Figure S.19 for details.

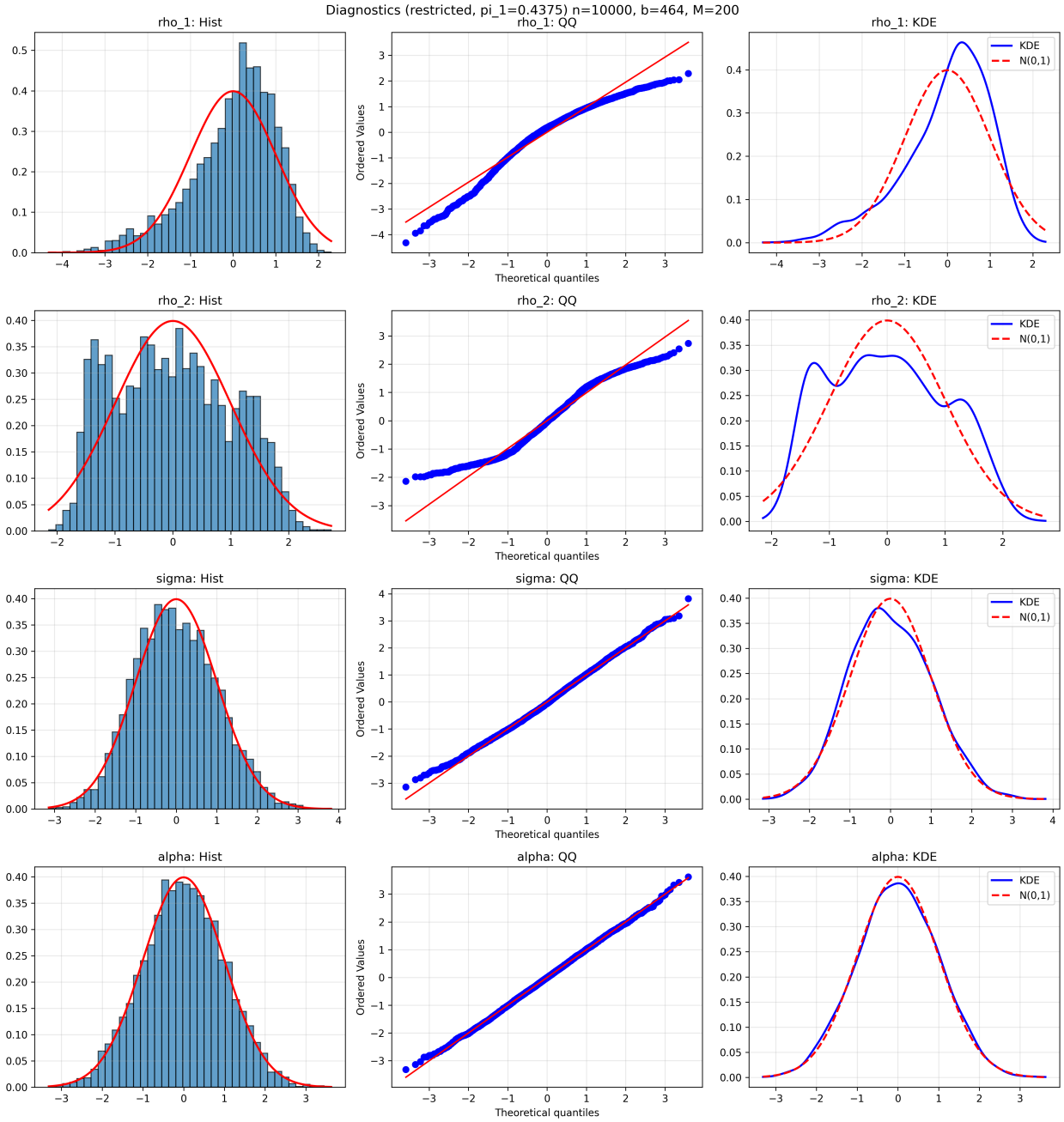

Figure S.22: Diagnostic plots for restricted subsampling ($\pi_1 = 0.4375$) at $n = 10,000$. See caption to Figure S.19 for details. .

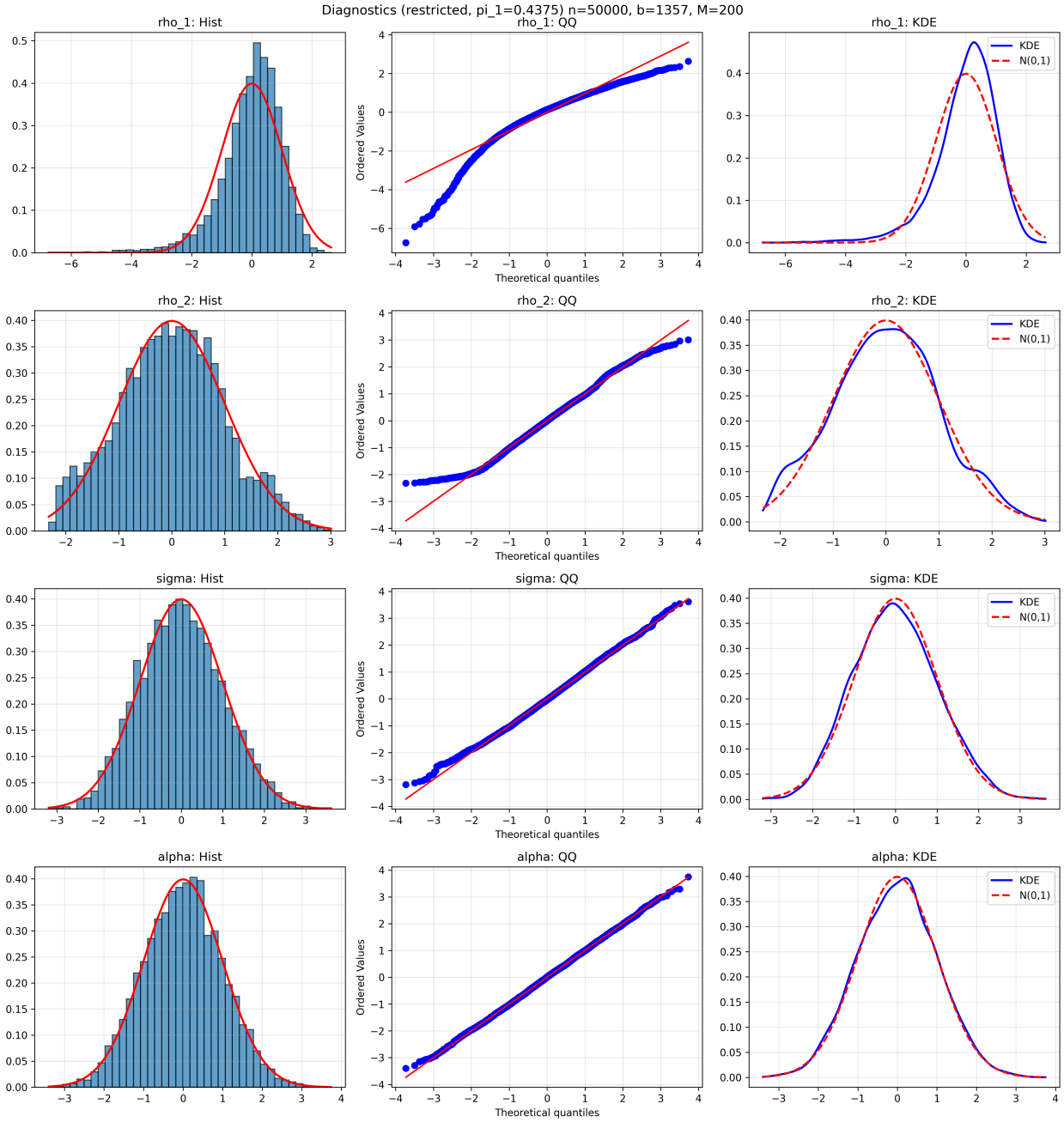

Figure S.23: Diagnostic plots for restricted subsampling ($\pi_1 = 0.4375$) at $n = 50{,}000$. See caption to Figure S.19 for details.

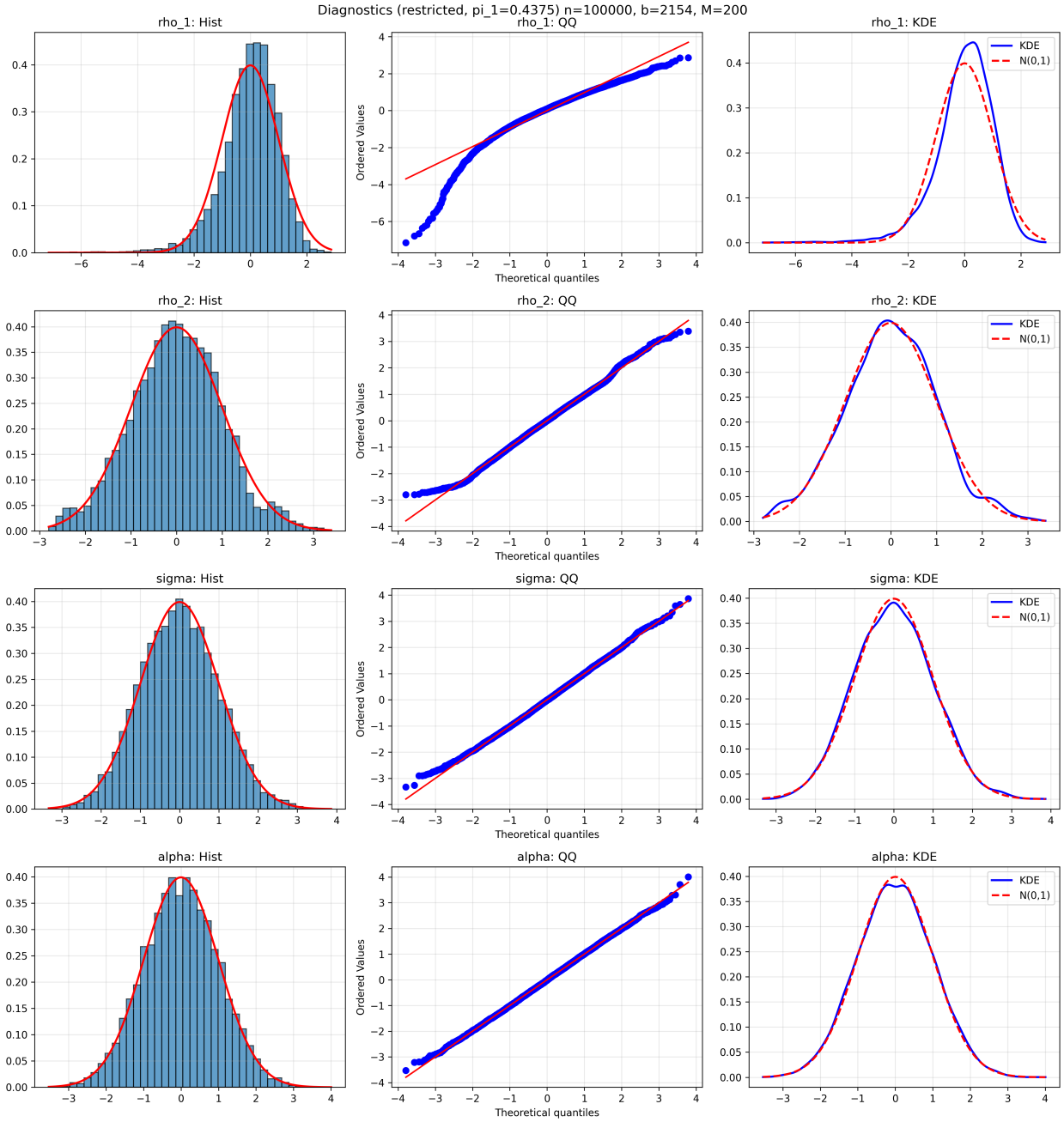

Figure S.24: Diagnostic plots for restricted subsampling ($\pi_1 = 0.4375$) at $n = 100{,}000$. See caption to Figure S.19 for details.

S.2. Per-component forecast details for the OVX application

This section provides the detailed in-sample forecasting results for the 2020 OVX bubble episode that were summarized in Section 5 of the main paper. We present the complete forecasting algorithm, the full prediction table with crash/survival probabilities for both latent components, and per-component crash probability profiles and forecast trajectories across three risk thresholds (90%, 95%, 99%). We also provide the extended discussion of the OVX decomposition and its implications for risk management in commodity markets.

S.2.1. Detailed interpretation of the OVX decomposition

The OVX decomposition reveals distinct bubble dynamics that highlights the heterogeneous nature of oil market volatility expectations captured by the stable aggregate framework. As evident from Figure 5 of the main paper, the first component ($\hat{\rho}_1 = 0.7989$, $\hat{\pi}_1 = 0.2790$) and the second component ($\hat{\rho}_2 = 0.8470$, $\hat{\pi}_2 = 0.7210$) exhibit markedly different contributions to extreme volatility episodes. The dramatic spike observed during the 2020 oil market disruption demonstrates how both components work in tandem to generate the observed market stress, with each capturing distinct aspects of investor fear and anticipation.

The first component, characterized by moderate persistence ($\hat{\rho}_1 = 0.7989$) and lower weight ($\hat{\pi}_1 = 0.28$), captures more transient but significant volatility movements, as evidenced by its sharp but relatively brief contribution to the 2020 crisis. In contrast, the second component, with higher persistence ($\hat{\rho}_2 = 0.8470$) and dominant weight ($\hat{\pi}_2 = 0.72$), represents the sustained underlying tension in oil markets that builds more gradually but contributes more substantially to prolonged periods of elevated volatility expectations.

This decomposition provides valuable insights for risk management in commodity markets, revealing that what appears as a single volatility episode actually comprises multiple superimposed processes with heterogeneous growth rates and crash probabilities. The ability to disentangle these distinct dynamics demonstrates the practical value of the stable aggregate modeling approach for energy market applications, enabling practitioners to distinguish between different sources of market stress—rapid panic responses versus slow-building fundamental concerns—and tailor their risk management strategies accordingly. The dominance of the second component ($\hat{\pi}_2 = 0.72$) suggests that persistent, slow-building volatility expectations are the primary driver of oil market fear, while the first component captures shorter-lived but equally important shock responses to unexpected market developments.

S.2.2. Forecasting algorithm

Our prediction strategy rests on the theoretical result of Proposition 3.3 of the main paper: during an extreme event, the trajectory of the aggregate process concentrates around a specific normalized pattern $\vartheta \boldsymbol{d}_{j_0,k}/\|\boldsymbol{d}_{j_0,k}\|$. The approach is fundamentally based on pattern recognition, exploiting the theoretical finding that during extreme events, trajectories adhere to specific patterns characterized by the normalized

form $\vartheta \boldsymbol{d}_{j,k}/\|\boldsymbol{d}_{j,k}\|$. These pattern structures are defined by four essential elements: the shape derived from the coefficient sequence $\boldsymbol{d}_{j,k}$; the component index $j \in \{1, \ldots, J\}$ identifying which latent process is driving the event; the time shift $k_0 \in \mathbb{Z}$ indicating the position within the pattern; and the sign $\vartheta \in \{-1, +1\}$ reflecting upward or downward movements.

The four-step algorithm proceeds as follows.

1. **Observation.** Observe the initial $m+1$ observations of the emerging extreme event ($m = 20$ throughout).
2. **Pattern matching.** Match the observed trajectory to the collection of theoretical patterns derived from the estimated $\mathcal{G}\alpha\mathcal{S}$ model, thereby identifying the component index j_0, the time shift k_0, and the sign ϑ_0. Each component generates a finite collection of potential patterns that an extreme event might follow, and Proposition 3.3 provides explicit formulas for calculating the conditional probabilities of future trajectories given an observed pattern.
3. **Probability computation.** For each future horizon $h \geq 1$, compute:

$$\mathbb{P}(\text{crash at } h) = |\rho_{j_0}|^{\alpha k}(1 - |\rho_{j_0}|^{\alpha}),$$
$$\mathbb{P}(\text{survive beyond } h) = |\rho_{j_0}|^{\alpha h},$$

   using $\hat{\rho}_{j_0}$ and $\hat{\alpha}$ from Table 5 of the main paper. For a bubble identified as originating from component j_0 (see the deconvolution in Figure 5 of the main paper), these formulas provide precise probabilistic forecasts of its future trajectory. The probability of the bubble crashing in exactly k periods is given by $|\rho_{j_0}|^{\alpha k}(1 - |\rho_{j_0}|^{\alpha})$, while the probability of surviving at least h periods is $|\rho_{j_0}|^{\alpha h}$. The growth rate of the bubble is determined by $\rho_{j_0}^{-1}$, which allows for trajectory forecasting once the component is identified.
4. **Forecast generation.** Given a risk threshold $p \in \{0.90, 0.95, 0.99\}$, forecast the trajectory $\hat{\rho}_{j_0}^{-(h-k_0)} \cdot X_{t_0}$ until $1 - |\rho_{j_0}|^{\alpha h} > p$, at which point the crash is predicted.

For the 2020 episode, the cut-off date is January 2020. Pattern matching yields $k_0 = 3$ for Component 1 ($\hat{\rho}_1 = 0.7989$) and $k_0 = 1$ for Component 2 ($\hat{\rho}_2 = 0.8470$).

S.2.3. In-sample prediction table

Table S.27 reports the predicted trajectory values, crash probabilities, and survival probabilities at each weekly horizon for both components, from the January 2020 cut-off through May 2020.

For Component 1 ($k_0 = 3$), we identify that from the start date through the third period, the crash has not yet occurred with certainty. Computing crash and survival probabilities for these early periods is therefore not meaningful, as the probability of a crash during this period is effectively zero by construction of the matched pattern. Only beginning at $h = 3$ do the crash probabilities become relevant; the bubble trajectory escalates from 11.27 to 208.73 over 13 periods before the 99% crash threshold is crossed at $h = 14$.

Table S.27: In-sample bubble forecast: predicted values and crash/survival probabilities (cut-off: January 2020, risk threshold: 99%).

		Component 1 ($k_0 = 3$, $\hat{\rho}_1 = 0.7989$)			Component 2 ($k_0 = 1$, $\hat{\rho}_2 = 0.8470$)		
Date	h	Forecast	Crash at h	Survive at h	Forecast	Crash at h	Survive at h
2020-01-05	0	11.2714	–	–	11.2714	–	–
2020-01-12	1	14.1087	–	–	13.3068	0.2164	0.7836
2020-01-19	2	17.6601	–	–	15.7098	0.3859	0.6141
2020-01-26	3	22.1056	0.6281	0.3719	18.5467	0.5188	0.4812
2020-02-02	4	27.6701	0.7326	0.2674	21.8958	0.6229	0.3771
2020-02-09	5	34.6325	0.8077	0.1923	25.8498	0.7045	0.2955
2020-02-16	6	43.3537	0.8617	0.1383	30.5178	0.7684	0.2316
2020-02-23	7	54.2668	0.9006	0.0994	36.0288	0.8185	0.1815
2020-03-01	8	67.9270	0.9285	0.0715	42.5349	0.8578	0.1422
2020-03-08	9	85.0258	0.9486	0.0514	50.2159	0.8886	0.1114
2020-03-15	10	106.4287	0.9630	0.0370	59.2839	0.9127	0.0873
2020-03-22	11	133.2193	0.9734	0.0266	69.9890	0.9316	0.0684
2020-03-29	12	166.7534	0.9810	0.0190	82.6283	0.9464	0.0536
2020-04-05	13	208.7292	0.9865	0.0135	97.5494	0.9580	0.0420
2020-04-12	14	0.0000*	0.9901	0.0099	115.1651	0.9671	0.0329
2020-04-19	15	0.0000*	0.9929	0.0071	135.9617	0.9742	0.0258
2020-04-26	16	0.0000*	0.9949	0.0051	160.5139	0.9798	0.0202
2020-05-03	17	0.0000*	0.9963	0.0037	189.4997	0.9842	0.0158
2020-05-10	18	0.0000*	0.9974	0.0026	223.7200	0.9876	0.0124
2020-05-17	19	0.0000*	0.9981	0.0019	0.0000*	0.9903	0.0097

Notes: Crash at h denotes $|\rho_{j_0}|^{\alpha k}(1 - |\rho_{j_0}|^{\alpha})$; Survive at h denotes $|\rho_{j_0}|^{\alpha h}$. *Crash predicted before this horizon at the 99% threshold (Component 1: $h = 14$; Component 2: $h = 19$). Forecast values after the predicted crash are set to zero. The pattern matching window is $m = 20$.

For Component 2 ($k_0 = 1$), crash probabilities are immediately non-negligible (0.22 at $h = 1$), reflecting the more immediate nature of bubbles generated by this component despite its higher persistence. Yet the lower growth rate $\hat{\rho}_2^{-1}$ sustains the trajectory through 18 periods, reaching 223.7 before the 99% threshold is crossed at $h = 19$.

S.2.4. Risk threshold and the precision/conservatism trade-off

A critical element in the forecasting framework is the risk threshold parameter, which allows practitioners to customize predictions according to their risk tolerance. Specifically, analysts using our procedure can select an acceptable probability threshold, such as 90%, 95%, or 99%, to determine when a bubble is likely to crash. When the cumulative crash probability $\mathbb{P}(\text{crash within } k \text{ periods}) = 1 - |\rho_{j_0}|^{\alpha k}$ exceeds this threshold, the model predicts a crash; otherwise, it anticipates continued growth. This flexibility in threshold selection creates a natural trade-off: higher thresholds (e.g., 99%) generate more extreme bubble projections before predicting a crash, while lower thresholds (e.g., 90%) produce more conservative forecasts

with earlier predicted crash points.

For Component 1, the predicted crash horizon shifts from $h = 7$ at the 90% threshold to $h = 14$ at the 99% threshold. For Component 2, the shift is from $h = 11$ to $h = 19$. In both cases, the 99% forecast trajectory most closely tracks the realized 2020 OVX path, as visible in the combined forecast of Figure 6 in the main paper.

S.2.5. Per-component crash probability profiles and forecasts

Figures S.25 and S.26 display, for each component separately, the crash probability profiles and zoomed-in trajectory forecasts across the three risk thresholds (90%, 95%, 99%). Each figure is organized in three rows: the top row shows the crash/survival/cumulative probability curves as a function of horizon h; the middle row shows zoomed forecast trajectories; the bottom row situates the forecast within the full 2015–2025 sample.

Figures S.25 and S.26 illustrate how the risk threshold impacts forecast accuracy. The first component ($\hat{\rho}_1 = 0.7989$), with its slightly lower persistence, captures more abrupt movements: its contribution to the 2020 crisis is sharp but relatively brief, and the 99% threshold trajectory escalates from 11.27 to 208.73 before the predicted crash. The second component ($\hat{\rho}_2 = 0.8470$), with its higher persistence and dominant weight, tracks the more sustained explosive patterns: its trajectory reaches higher absolute values (up to 223.7) before the predicted collapse, reflecting the longer-lived nature of the underlying market anxiety.

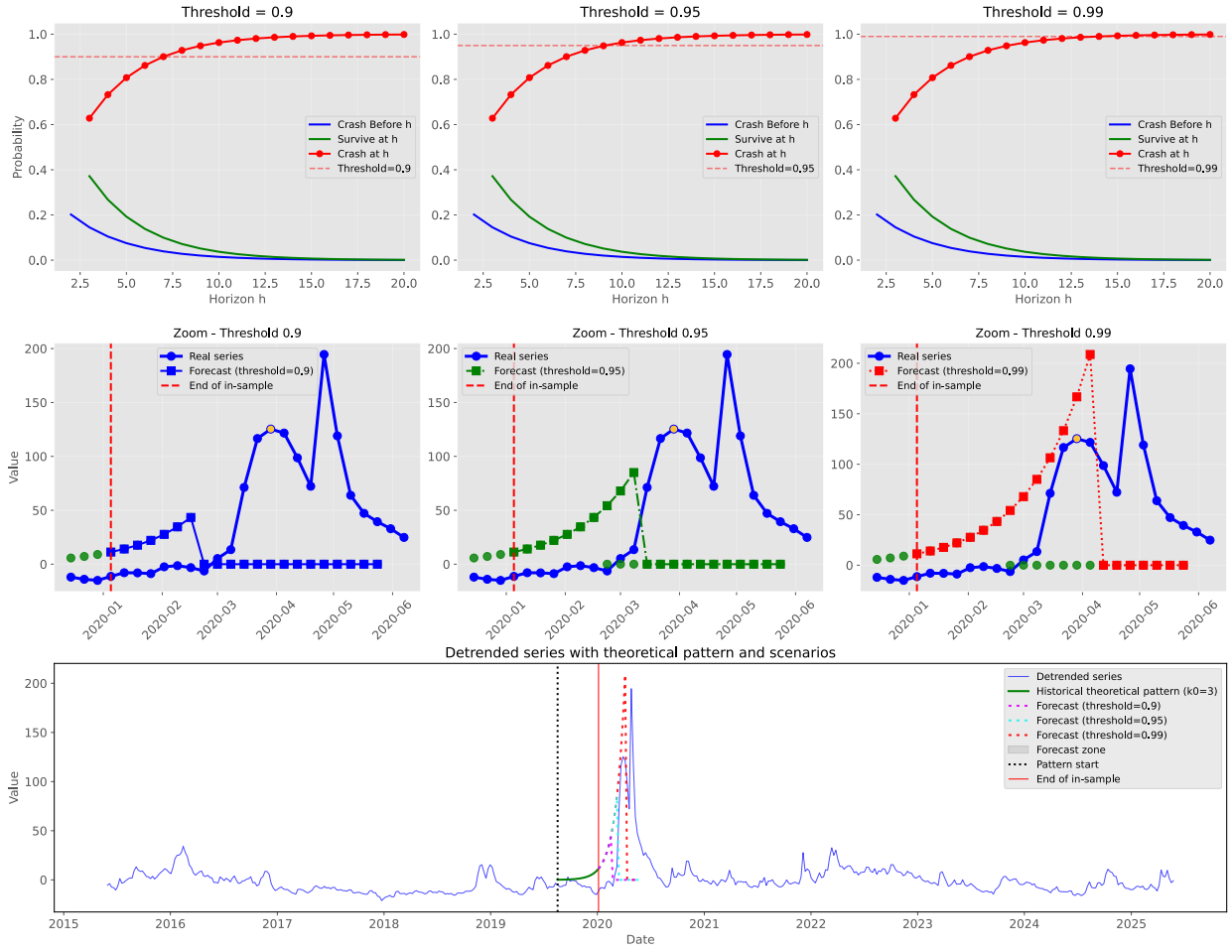

Figure S.25: In-sample forecast for the 2020 OVX bubble: Component 1 ($\hat{\rho}_1 = 0.7989$, $k_0 = 3$). *Top row:* crash probability profiles for risk thresholds 0.90 (left), 0.95 (center), and 0.99 (right). Each panel shows the probability of crashing at a given date (red line with circles), surviving beyond that date (green line), the cumulative crash probability (blue line), and the threshold (horizontal dashed red line). *Middle row:* zoomed-in forecast trajectories for each threshold; colored squares are predicted values; vertical dashed red line marks the cut-off (January 2020). *Bottom row:* full-sample view with the matched historical theoretical pattern ($k_0 = 3$) in green; forecasts at 0.90 (yellow), 0.95 (green dashed), and 0.99 (red dashed) thresholds; shaded area is the forecast zone. Pattern matching window: $m = 20$.

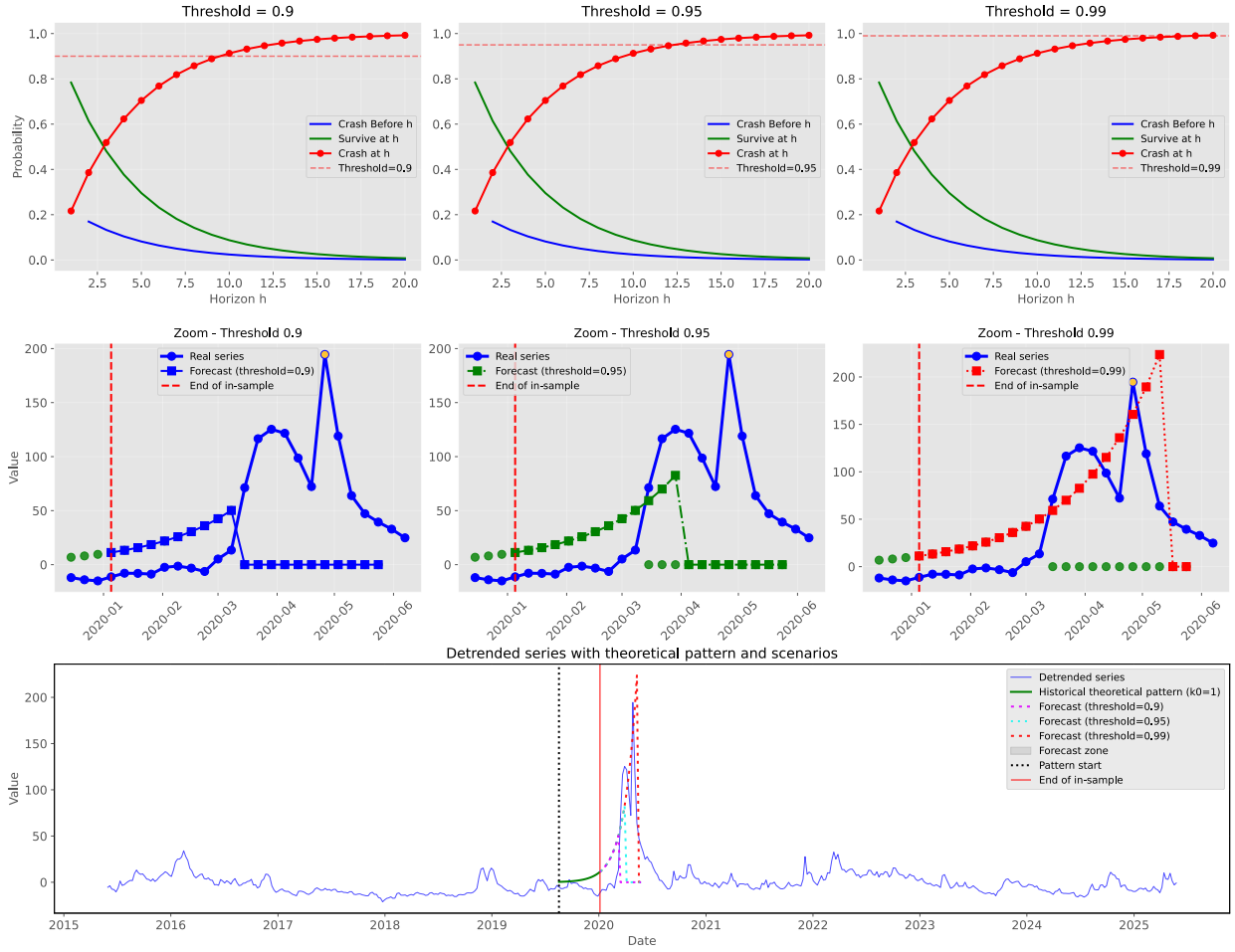

Figure S.26: In-sample forecast for the 2020 OVX bubble: Component 2 ($\hat{\rho}_2 = 0.8470$, $k_0 = 1$). Layout identical to Figure S.25. The historical theoretical pattern ($k_0 = 1$) is shown in green in the bottom row. Compared to Component 1, crash probabilities build more gradually but the forecasted trajectory reaches higher absolute values before the predicted crash, reflecting the higher persistence and dominant weight ($\hat{\pi}_2 = 0.72$) of this component. Pattern matching window: $m = 20$.

References

Politis, D.N., and J.P., Romano. 1994. Large Sample Confidence Regions Based on Subsamples under Minimal Assumptions. *The Annals of Statistics*, 22(4), 2031–2050.

Politis, D.N., Romano, J.P., and M., Wolf. 1999. *Subsampling*. Springer.

de Truchis, G., Thomas, A., L. Vaudrée (2025). Deconvolution and Filtering of Non-Causal Alpha-Stable Processes. *On going paper*.